Theoret. Comput. Fluid Dynamics (1995) 7: 49–76

Theoretical and Computational Fluid Dynamics

Spatial Direct Numerical Simulation of High-Speed Boundary-Layer Flows Part I: Algorithmic Considerations and Validation

C. David Pruett

Analytical Services & Materials, Inc., Hampton, VA 23666, U.S.A.

Thomas A. Zang

Computational Sciences Branch, NASA Langley Research Center, Hampton, VA 23681, U.S.A.

Chau-Lyan Chang

High Technology Corporation, Hampton, VA 23665, U.S.A.

Mark H. Carpenter

Theoretical Flow Physics Branch, NASA Langley Research Center, Hampton, VA 23681, U.S.A.

Communicated by M.Y. Hussaini

Received 6 May 1993 and accepted 13 August 1993

Abstract. A highly accurate algorithm for the direct numerical simulation (DNS) of spatially evolving high-speed boundary-layer flows is described in detail and is carefully validated. To represent the evolution of instability waves faithfully, the fully explicit scheme relies on non-dissipative high-order compact-difference and spectral collocation methods. Several physical, mathematical, and practical issues relevant to the simulation of high-speed transitional flows are discussed. In particular, careful attention is paid to the implementation of inflow, outflow, and far-field boundary conditions. Four validation cases are presented, in which comparisons are made between DNS results and results obtained from either compressible linear stability theory or from the parabolized stability equation (PSE) method, the latter of which is valid for nonparallel flows and moderately nonlinear disturbance amplitudes. The first three test cases consider the propagation of two-dimensional second-mode disturbances in Mach 4.5 flat-plate boundary-layer flows. The final test case considers the evolution of a pair of oblique second-mode disturbances in a Mach 6.8 flow along a sharp cone. The agreement between the fundamentally different PSE and DNS approaches is remarkable for the test cases presented.

1. Introduction

A worthy "grand challenge" for the computational boundary-layer-transition community is the accurate direct numerical simulation (DNS) of the complete laminar-turbulent transition process in a spatially evolving high-speed boundary-layer flow. Even for such simple geometries as the flat plate or

sharp cone, this remains a daunting goal. It was only in the late 1980s that the corresponding challenge for temporally evolving incompressible flow was met by Gilbert and Kleiser (1990) for the relatively simple problem of channel-flow transition. For spatially evolving compressible boundary-layer flows, the recent landmark simulations of Rai and Moin (1991) and Thumm (1991) have come closest to the realization of this goal. In the former simulation a fully turbulent state was attained from an initially laminar state subject to high-amplitude random forcing imposed in the free stream. However, although the algorithm was designed for compressible flow, the low subsonic Mach number (Mach 0.1) of the numerical experiment guaranteed that the flow was essentially incompressible in behavior. The latter computation of Thumm (1991) considered a relatively low-speed supersonic flow (Mach 1.6), and, while simulating highly nonlinear stages of transition, it did not proceed into a fully turbulent regime. (For a thorough background of DNS for transitional incompressible and compressible wall-bounded flows, including a discussion of the temporal and spatial problems, see Kleiser and Zang (1991).)

The first tentative steps were taken in the use of DNS to investigate transition to turbulence in supersonic, wall-bounded flows in the mid to late 1980s. Bayliss *et al.* (1985) presented the first DNS results for supersonic boundary-layer flow along a flat plate. These results were for spatially evolving, but two-dimensional, flow. The first three-dimensional DNS of a perturbed high-speed (Mach 4.5) flat-plate boundary-layer flow was accomplished by Erlebacher and Hussaini (1990). This numerical experiment used temporal DNS to examine boundary-layer stability, but stopped far short of attaining a transitional state.

Recently, due partly to increased supercomputer capacity, there have been many noteworthy three-dimensional simulations of compressible wall-bounded flows. Among these are temporal simulations by Normand and Lesieur (1992), Pruett and Zang (1992), Dinavahi and Pruett (1993), and Adams and Kleiser (1993); and spatial simulations by Thumm *et al.* (1990), Maestrello *et al.* (1991), Thumm (1991), Normand and Lesieur (1992), Eissler and Bestek (1993), Ng and Zang (1993), and Pruett and Chang (1993). Among these, the temporal simulation of Dinavahi and Pruett (1993) is unique in attaining a well-resolved fully turbulent state without recourse to modeling.

To date, with the exception of Rai and Moin (1991), virtually all of the numerical experiments cited have simulated controlled rather than natural instability processes. In a controlled experiment, instability waves of a particular wavelength (temporal) or frequency (spatial) are excited by imposed forcing. In contrast, in natural transition the input is random, and the flow itself selects the preferred instability modes. A few of the cited simulations are hybrid in the sense that the primary instability wave is imposed, whereas secondary instability is triggered by low-level noise. A distinguishing feature of high-speed boundary-layer flows is that multiple primary instability modes can coexist (Mack, 1984). The viscous first-mode instability, the counterpart of the Tollmien–Schlichting (TS) wave in incompressible flow, predominates in low-speed compressible flows. In hypersonic boundary-layer flows second-mode instabilities arise, which are acoustic in nature, and which eventually predominate as the Mach number increases. Thus far, all simulations of instability and transition in compressible flows have focused on first- and second-mode instabilities and their associated secondary instabilities, rather than on crossflow or Goertler modes.

Several observations gleaned from temporal DNS are worthy of note. Normand and Lesieur (1992) performed both DNS of a low-speed (Mach 0.5) compressible flat-plate flow and large-eddy simulation of a high-speed (Mach 5) flow. They observed transition to occur by means of fundamental secondary instability in the former case and subharmonic secondary instability in the latter case. Their findings are consistent with those of Pruett and Zang (1992), Dinavahi and Pruett (1993), and Adams and Kleiser (1993). Pruett and Zang (1992) and Dinavahi and Pruett (1993) considered the case or Mach 4.5 flow along a hollow cylinder (the axisymmetric analog of a flat-plate boundary layer) and observed subharmonic secondary instability triggered by second-mode primary instability to lead to transition. Adams and Kleiser (1993) performed a similar computation for a Mach 4.5 fat plate using random noise to trigger secondary instability from a base state perturbed by a second-mode disturbance. The secondary instabilities they observe are of subharmonic type and agree in growth rate and structure with the predictions of temporal secondary instability theory (Ng and Erlebacher, 1992). Moreover, despite the difference in geometry, their results are in qualitative agreement with those of Pruett and Zang (1992). A potential weakness of each of these simulations, however, is the failure to

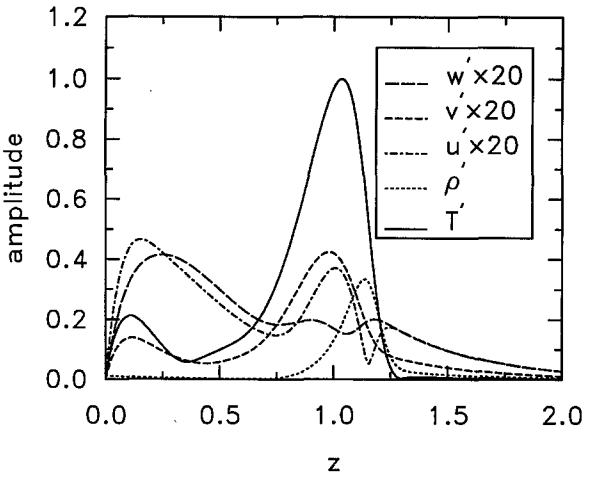

Figure 1. Amplitudes of components of oblique second-mode disturbance of $F = 2.094 \times 10^{-4}$ and $Re_L = 1013$ in Mach 6.8 boundary layer on 7° sharp cone.

account for growth of the boundary layer, a somewhat ambiguous task in the context of temporal theory. Recent experimental results (Stetson and Kimmel, 1993) and numerical results obtained from the parabolized-stability-equation (PSE) method (Chang, 1993) suggest that subharmonic secondary instability may not be the preferred path to transition in a growing high-speed boundary layer. The issue can probably only be resolved by spatial DNS, which incorporates the evolution of the boundary layer.

The temporal simulations cited above required upward of 10^6 grid points and consumed hundreds of Cray Y-MP CPU hours. There are several reasons for the great expense of computations of high-speed compressible flow relative to simulations of incompressible or subsonic flows:

1. The time discretizations in the compressible cases were fully explicit. In many instances the allowable time step was limited by the viscous stability condition rather than by the advection condition. For incompressible simulations the viscous stability limit is usually absent due to the conventional implicit treatment of the viscous terms.
2. The second-mode disturbances associated with high-speed transitional flows have a double-peaked structure (Figure 1) with amplitude peaks occurring both near the wall and the critical layer ($z \approx 1$ in Figure 1). In contrast to low-speed flows, at high speeds the critical layer lies far (approximately one displacement thickness) from the wall, necessitating concentrations of grid points in both regions of strong gradients.
3. At high speeds the growth rates of both the primary and secondary instabilities are much slower than for low-speed flows. This requires much longer time integrations.
4. In contrast to DNS of incompressible flow, flow-field oscillations due to inadequate resolution are potentially fatal in the compressible case since spurious negative densities, pressures, and/or temperatures can arise.

Relative to temporal DNS, spatial DNS is yet more computationally demanding, primarily because of the greater length of the computational domain. Nonetheless, the computational boundary-layer transition community has recently produced several spatial simulations of particular importance. The simulations of Thumm *et al.* (1990) examine the very early stages of secondary instabilities of both fundamental and subharmonic type in Mach 1.6 boundary-layer flows along a flat plate. Subsequently, Thumm (1991) turned his attention to investigating a new "oblique-mode" transition mechanism, again for Mach 1.6 flat-plate flow. Conventionally, transition is triggered by secondary instability originating from a finite-amplitude two-dimensional primary disturbance and a pair (or array) of low-amplitude oblique secondary disturbances. For Mach 1.6 boundary-layer flow, however, the most amplified linear instability turns out to be oblique and not two-dimensional, in contrast to the case for either incompressible flow or flow at very high Mach numbers. This suggests the possibility of triggering transition simply by the nonlinear interactions of a pair of symmetric unstable primary modes. Thumm (1991) presented an extensive set of results, comparing fundamental-, subharmonic-,

and oblique-breakdown scenarios. The simulations, which were carried into the early nonlinear stages of laminar breakdown, have recently been summarized by Fasel *et al.* (1993). Maestrello *et al.* (1991) performed three-dimensional spatial simulations of Mach 4.5 flows excited simultaneously by a two-dimensional second-mode disturbance and a single oblique disturbance of the same frequency. They computed to the early nonlinear stages of transition and demonstrated significant interactions between the forced modes, which then generated other rapidly growing instability modes. Eissler and Bestek (1993) performed several simulations at Mach 4.8 using periodic suction and blowing at the wall to excite instability waves. In addition to the excitation of the expected oblique second mode, their results showed excitation of an additional "viscous" mode of the same frequency but of different wavelength. The evolution of these modes was tracked from the first-mode region into the second-mode region.

Of these simulations, the typical spatial accuracy was fourth-order, occasionally with a spectrally accurate Fourier collocation method in the (periodic) spanwise direction. In most of these spatial simulations the spanwise resolution was modest, in some cases admitting just a single oblique mode. Although Thumm (1991) used up to 17 grid points in the spanwise direction, and Maestrello *et al.* (1991) used up to 32 spanwise grid points, such resolution is believed to be insufficient for the later stages of transition, in which there is typically an explosive broadening in wave space of the energy spectrum in the spanwise direction. The simulations at the higher Mach numbers call attention to the difficulties (and impracticality) of simulating the entire laminar-turbulent transition process when the dominant second-mode instabilities are of high frequency but slow growth. To begin from a linearly perturbed laminar state, the computational domain must be extremely long in streamwise extent (relative to the disturbance wavelength). Alternately, the forcing amplitudes must be quite large, in which case nonlinear interactions are significant at the inflow boundary and consistent inflow conditions are difficult to obtain.

This work focuses on the development of an algorithm and additional procedures for which spatial DNS of such challenging high-speed transition problems is feasible. With regard to the algorithm, its origins can be found in Ng and Zang (1993), who compared spatial DNS with secondary instability predictions for Mach 1.6 and Mach 6.8 flows in artificial, quasi-parallel boundary-layer flows. Their work validated both the basic spatial DNS code and the spatial secondary instability code, but it was not an investigation into the physics of transition. Their work, however, formed the starting point for the algorithm developed by Pruett and Chang (1993) for the spatial DNS computations and the results reported in this paper. Pruett and Chang (1993) made detailed comparisons of spatial DNS and PSE for two-dimensional linear and nonlinear second-mode disturbances in Mach 4.5 flat-plate boundary layers. They achieved remarkable agreement between the methods for these cases; however, they found that the numerical methods utilized in the DNS had to be extremely refined in order to obtain accurate results. Careful attention was given to many details often overlooked. Among the issues addressed were: obtaining self-consistent inflow conditions for nonparallel flows, the necessity of filtering to suppress spurious high-frequency modes and boundary reflections, obtaining reliable estimates for the numerical stability limits on the time step as a function of the precise spatial discretization, and the imposition of nonreflecting far-field and outflow boundary conditions.

Our present position is that the "grand challenge" of simulating transition in high-speed boundary-layer flows is best met by a combination of numerical tools. The PSE method is much more efficient than DNS for computing the early linear and weakly nonlinear stages of the transition process. Thus, we advocate the use of PSE to furnish accurate and consistent inflow conditions to a DNS that commences near the highly nonlinear laminar-breakdown stage. The primary objective of this paper is to provide thorough validation and documentation of the DNS algorithm. In the cross-validation of DNS with PSE, however, we demonstrate convincingly the fidelity of the PSE method within the appropriate flow regimes.

An alternative, but still developing approach, is that of large-eddy simulation (LES). In this method large-scale structures are resolved, but a model is employed for the subgrid-scale fluctuations. The LES approach is fairly well developed for incompressible flows (see Kleiser and Zang, 1991), but only a few results are available for supersonic flows (see Normand and Lesieur, 1992; Zang *et al.*, 1992; El-Hady *et al.*, 1993). Because the cost of PSE increases much faster than that of DNS as the number of spanwise modes is increased, PSE is limited in practice to investigations of narrow-band forcing. At present, LES appears to be the only hope for complete simulations of natural (broad-band)

transition. In the same way that the spatial DNS described herein has served to validate PSE, it is hoped that it will also be useful in validating LES approaches.

This paper consists of a reprise of the Pruett and Chang (1993) results, with an emphasis on the subtle numerical issues that are essential for accurate spatial DNS of high-speed boundary-layer flows. Their previous work is also extended to the simulation of three-dimensional second-mode disturbances propagating in the boundary layer of a sharp cone immersed in a Mach 8 flow. The motivation for this example is the stability experiment by Stetson *et al.* (1983), in which the second-mode disturbance was observed as the dominant instability in such a flow. The ultimate objective of this work, and the subject of the sequel to this paper, is the combined PSE/DNS investigation of the complete laminar-turbulent transition process in a hypersonic boundary-layer flow along a cone.

In the next section the three-dimensional compressible Navier–Stokes equations are presented for flow along a two-dimensional or an axisymmetric body. The fully explicit numerical method, which combines high-order compact-difference and spectral collocation methods, is presented in detail in Section 3. Algorithm details are discussed in Section 4. In Section 5 compressible linear stability theory (LST) and the PSE method are discussed very briefly, and the DNS code is thoroughly validated against these yardsticks. Three of the four validation cases examine the evolution of two-dimensional second-mode instability waves in a Mach 4.5 flat-plate boundary-layer flow. Both linear and nonlinear disturbance amplitudes are considered. The fourth case examines the evolution of a pair of oblique second-mode disturbances on a sharp 7° half-angle cone in a Mach 6.8 (free-stream Mach 8) flow. Conclusions which relate both to the numerical method and to transition physics are presented in the final section.

2. Governing Equations

Consider the body-fitted orthogonal coordinate system $\mathbf{x} = [x, \theta, z]^T$ on an axisymmetric body as shown in Figure 2, where x is the arc length along the body, θ is the azimuthal angle, and z is the coordinate normal to the body. Associated with $\mathbf{x}$ is the fundamental metric tensor g_{mn}, which has the nonzero components

$$g_{11} = s^2, \qquad g_{22} = r^2, \qquad g_{33} = 1, \tag{1}$$

where

$$\begin{aligned} r(x, z) &= R + z\cos\varphi, \\ s(x, z) &= 1 - z\frac{d\varphi}{dx}, \end{aligned} \tag{2}$$

and where $R(x)$ and $\varphi(x)$ are the body radius and the angle of the surface tangent in the plane of symmetry, respectively. For convenience, we define the following partial differential operators, which incorporate the metric quantities r and s:

$$D_x^0 u \equiv \frac{1}{s}\frac{\partial u}{\partial x}, \qquad D_\theta^0 u \equiv \frac{1}{r}\frac{\partial u}{\partial \theta}, \qquad D_z^0 u \equiv \frac{\partial u}{\partial z}, \qquad D_x^1 u \equiv \frac{1}{rs}\frac{\partial (ru)}{\partial x}, \qquad D_z^1 u \equiv \frac{1}{rs}\frac{\partial (rsu)}{\partial z}. \tag{3}$$

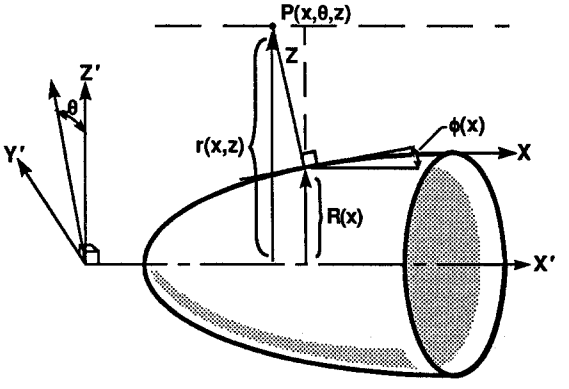

Figure 2. Body-fitted coordinate system on axisymmetric body.

In the coordinate system of Figure 2 and in the terminology of (3), the dimensionless compressible Navier–Stokes equations assume the following conservative form:

$$\frac{\partial \mathbf{Q}}{\partial t} + D_x^1 \mathbf{E} + D_\theta^0 \mathbf{F} + D_z^1 \mathbf{G} + \mathbf{H} = \mathbf{0}, \tag{4}$$

where $\mathbf{Q} = [\rho, \rho u, \rho v, \rho w, E_t]^T$ is the fluid state vector of conserved quantities; ρ is the density; u, v, and w are velocities in the $\mathbf{e}_x$, $\mathbf{e}_\theta$, and $\mathbf{e}_z$ directions, respectively; and E_t is the total energy. For later use, we also define the vector of primitive variables $\mathbf{U} = [\rho, u, v, w, p]^T$, and, for state and flux vectors in general, $\mathbf{Q} = [Q_0, Q_1, Q_2, Q_3, Q_4]^T$, etc. Vectors **E**, **F**, **G**, and **H** are defined as follows:

$$\mathbf{E} = \begin{bmatrix} \rho u \\ \rho uu - \tau_{11} - p \\ \rho uv - \tau_{12} \\ \rho uw - \tau_{13} \\ (E_t + p)u - u\tau_{11} - v\tau_{12} - w\tau_{13} - h_1 \end{bmatrix},$$

$$\mathbf{F} = \begin{bmatrix} \rho v \\ \rho vu - \tau_{21} \\ \rho vv - \tau_{22} - p \\ \rho vw - \tau_{23} \\ (E_t + p)v - u\tau_{21} - v\tau_{22} - w\tau_{23} - h_2 \end{bmatrix},$$

$$\mathbf{G} = \begin{bmatrix} \rho w \\ \rho wu - \tau_{31} \\ \rho wv - \tau_{32} \\ \rho ww - \tau_{33} - p \\ (E_t + p)w - u\tau_{31} - v\tau_{32} - w\tau_{33} - h_3 \end{bmatrix}, \tag{5}$$

$$\mathbf{H} = \begin{bmatrix} 0 \\ -\dfrac{\sin\varphi}{r} F_2 - (D_x^0 \varphi) E_3 \\ \dfrac{\sin\varphi}{r} F_1 + \dfrac{\cos\varphi}{r} F_3 \\ -\dfrac{\cos\varphi}{r} F_2 + (D_x^0 \varphi) E_1 \\ 0 \end{bmatrix},$$

where p is thermodynamic pressure,

$$h_1 = \frac{\kappa}{(\gamma - 1) M_r^2 Re} D_x^0 T,$$

$$h_2 = \frac{\kappa}{(\gamma - 1) M_r^2 Re} D_\theta^0 T, \tag{6}$$

$$h_3 = \frac{\kappa}{(\gamma - 1) M_r^2 Re} D_z^0 T$$

are the heat flux components, T is the temperature, κ is the thermal conductivity,

$$\tau_{ij} = \frac{2\mu}{Re} \sigma_{ij} - \frac{2}{3} \frac{\mu}{Re} \delta_{ij} d \tag{7}$$

is the stress tensor, μ is the dynamic viscosity, δ_{ij} is the Kronecker delta, $d = D_x^1 u + D_\theta^0 v + D_z^1 w$ is the divergence of the velocity (dilatation), and σ_{ij} is the symmetric rate-of-deformation tensor with

components

$$\sigma_{11} = D_x^0 u - w D_x^0 \varphi,$$

$$\sigma_{22} = D_\theta^0 v + \frac{u \sin\varphi}{r} + \frac{w \cos\varphi}{r},$$

$$\sigma_{33} = D_z^0 w,$$

$$\sigma_{12} = \sigma_{21} = \tfrac{1}{2}\left(D_\theta^0 y + D_z^0 v - \frac{v \sin\varphi}{r}\right), \tag{8}$$

$$\sigma_{13} = \sigma_{31} = \tfrac{1}{2}(D_x^0 w + D_z^0 u - u D_x^0 \varphi),$$

$$\sigma_{23} = \sigma_{32} = \tfrac{1}{2}\left(D_\theta^0 w + D_z^0 v - \frac{v \cos\varphi}{r}\right).$$

With the exception of (1), which refers to a covariant tensor, all other equations refer to physical vector or tensor components. Thus, for convenience and brevity, we adopt a loose notation of referencing physical components by subscripts.

The components of vector (4) define, respectively, conservation of mass, conservation of momentum in the three dimensions, and conservation of energy. The governing system is closed by the equation of state. For this work, we assume that the fluid is air and behaves as a perfect gas, whereby

$$\gamma M_r^2 p = \rho T, \tag{9}$$

$$E_t = \frac{p}{\gamma - 1} + \frac{\rho}{2}(u^2 + v^2 + w^2), \tag{10}$$

and $\kappa = \mu/Pr$.

Four dimensionless parameters emerge from nondimensionalization: Mach number, Reynolds number, Prandtl number, and the ratio of specific heats, defined, respectively, as follows:

$$M_r = \frac{u_r^*}{\sqrt{\gamma R_g^* T_r^*}}, \qquad Re = \frac{\rho_r^* u_r^* \delta_{in}^*}{\mu_r^*}, \qquad Pr = \frac{C_p^* \mu_r^*}{\kappa_r^*}, \qquad \gamma = \frac{C_p^*}{C_v^*}, \tag{11}$$

where R_g^*, C_p^*, and C_v^* are the ideal gas constant and the specific heats at constant pressure and constant volume, respectively. Throughout this work, dimensional quantities are denoted by asterisk, reference values are denoted by a subscript "r", $Pr = 0.7$, and $\gamma = 1.4$. In the nondimensionalization from which (4) arises, the reference values for density, velocities, and temperature, ρ_r^*, u_r^*, and T_r^*, respectively, are arbitrary. Pressure is scaled by $\rho_r^* u_r^{*2}$. Viscosity is normalized by the viscosity at the reference temperature and is assumed to vary according to Sutherland's law. In dimensionless form

$$\mu = \frac{T^{3/2}(1 + C)}{T + C}, \qquad C = \frac{110.3\ \mathrm{K}}{T_r^*}. \tag{12}$$

Throughout this paper, a subscript "e" denotes a value at the boundary-layer edge, and lengths are scaled by the boundary-layer displacement thickness at the inflow boundary δ_{in}^*, where, in general (White, 1974),

$$\delta^*\left(1 + \frac{\delta^*}{2R^*}\right)^b = \int_0^\infty \left(\frac{r^*}{R^*}\right)^b \left(1 - \frac{\rho^* u^*}{\rho_e^* u_e^*}\right) dz^*, \qquad b = \begin{cases} 0, & \text{two-dimensional,} \\ 1, & \text{axisymmetric.} \end{cases} \tag{13}$$

For comparison with results obtained from spatial LST and the PSE method, we define the boundary-layer length scale as

$$L^* \equiv \sqrt{\frac{\mu_e^* x^*}{\rho_e^* u_e^*}}, \tag{14}$$

and we denote the Reynolds number based on edge conditions and L^* as Re_L. For comparisons with experiments, it is also useful to define Re_x, the Reynolds number based on x^*, whereby $Re_x = (Re_L)^2$.

With proper interpretation, (4) is valid for either two-dimensional or axisymmetric bodies. The two-dimensional case is recovered as $r \to 1$ in (3) and $1/r \to 0$ in **H** (5).

A nonconservative, but computationally useful, alternative form of the energy equation is

$$\begin{gathered} Q_4 = p, \qquad E_4 = pu, \qquad F_4 = pv, \qquad G_4 = pw, \\ H_4 = \Phi - (\gamma - 1)p\nabla\cdot\mathbf{u}, \qquad \Phi \equiv \sigma_{ij}\tau_{ij}, \\ \nabla\cdot\mathbf{u} \equiv D_x^1 u + D_\theta^0 v + D_z^1 w, \end{gathered} \tag{15}$$

where repeated indices imply summation. In subsequent discussions we refer to (15) as the "pressure equation" as distinguished from the "energy equation."

Mathematically, DNS is the numerical solution of an Initial-Boundary-Value Problem (IBVP). For spatial DNS, inflow and outflow boundary conditions are required. The imposition of initial and boundary conditions is discussed more fully in the next section.

3. Numerical Method

Navier–Stokes codes fall roughly into two classes depending upon the application: aerodynamic codes, in which body geometry is usually complicated, but from which one typically wants to extract only mean quantities such as surface pressure, lift, and drag; and DNS codes, in which body geometry is simple, but from which one wants to compute fine details of the flow field, ideally, to the smallest scales. Usually, aerodynamic codes are of relatively low-order accuracy, and, to capture shocks, they impose significant artificial dissipation through some form of upwinding. Often the boundary layer is severely underresolved, a deficiency partially atoned for by the use of transition or turbulence models. In contrast, in DNS, for which the boundary layer is the primary focus, dissipation and dispersion errors must be minimized if the growth rates and phase speeds of instability waves are to be computed accurately.

In this section, we present a fully explicit method designed specifically for the DNS of instability and transition in high-speed boundary-layer flows. The flow region of interest is downstream of the bow shock, and it is an implicit assumption that there are no shocks in the domain. To minimize dissipation and dispersion errors, we rely on a combination of spectral methods and high-order central compact-difference approximations for spatial derivatives. In the development of the algorithm, accuracy, efficiency, and simplicity, in that order, have been our guiding criteria.

Spatial Discretizations

We consider the physical domain and grid points defined by

$$\begin{aligned} x_{\text{in}} \le x_i \le x_{\text{out}}, \qquad & i = 0, \ldots, N_x, \\ 0 \le \theta_j \le \frac{2\pi}{n}, \qquad & j\ 0, \ldots, N_\theta, \\ 0 \le z_k \le z_{\max}, \qquad & k = 0, \ldots, N_z. \end{aligned} \tag{16}$$

Let u_{ijk} be the discrete approximation of $u(x_i, \theta_j, z_k)$, etc., and, for the moment, assume that grid points are equally spaced in terms of their respective coordinates. For DNS of axisymmetric (two-dimensional) boundary layers, it is conventional and physically reasonable to assume that the flow is periodic in the azimuthal (spanwise) direction. This periodicity permits the exploitation of spectral collocation methods (e.g., Canuto *et al.*, 1988) based on finite series expansions of the flow quantities in terms of Fourier basis functions, as, for example,

$$u(\mathbf{x}, t) = \sum_{j=-N_\theta/2}^{N_\theta/2} \hat{u}_j(x, z, t)\cdot\exp\{\imath jn\theta\}, \tag{17}$$

where $\imath = \sqrt{-1}$. Collectively, the Fourier coefficients $\hat{u}_j$ provide the Fourier spectrum, an intrinsic measure of the adequacy of resolution. The integer n, which appears in (16) and (17), is a parameter of the flow that defines the period in the azimuthal direction and is related to the azimuthal wave

number β through the relation

$$n = \beta r = \beta_0 R_0, \qquad R_0 \equiv R(x_{\text{in}}). \tag{18}$$

(For bodies on which the radius changes, such as a cone, (18) implies that the wave number of oblique (helical) waves evolves with x.) We implement the collocation method in the conventional pseudo-spectral manner. That is, derivatives with respect to θ of the truncated series in (17) are evaluated exactly in Fourier space, whereas nonlinear terms of the governing equations are evaluated in physical space. Vectorized fast Fourier transforms (FFTs) are used to shuttle efficiently between the transform and physical spaces. If desired, aliasing errors are controlled by spectral truncation. For computational efficiency, an option exists in the code to enforce symmetry about the plane $\theta = 0$, in which case odd (e.g., v) and even (e.g., u) functions are expanded in sine and cosine series, respectively, rather than in complex exponential series. As expected, there is roughly a factor of 2 reduction in computational effort with symmetry enforced.

The proper spectral expansion for a two-dimensional, rather than an axisymmetric, body is recovered from (17) by defining the azimuthal arc length $y = r\theta$ and by using (18).

For spatial DNS, both the streamwise and wall-normal directions are aperiodic, which precludes the use of Fourier spectral methods. In the aperiodic directions our DNS code allows a variety of differentiation options. Among these are a Chebyshev spectral-collocation scheme and several members from a class of fourth-order and sixth-order central compact-difference schemes (Lele, 1990; Carpenter *et al.*, (1991)). For explicit time advancement, the Chebyshev spectral method is subject to an extremely severe restriction on the time step of the form $\Delta t \sim 1/N_z^4$, which renders the method impractical for long-time integrations. Nevertheless, the method is useful for diagnostic purposes. In particular, it permits us to compute the Chebyshev spectrum as an indicator of the adequacy of resolution.

In the context of fully explicit time advancement, derivatives are computed by means of compact-difference techniques as follows:

$$M\mathbf{u}_z = E\mathbf{u}, \tag{19}$$

where M is a tridiagonal matrix, E is a banded matrix, and the vector $\mathbf{u}_z$, for example, contains the discrete approximation of $\partial u/\partial z$. Matrices M and E are referred to as the implicit and explicit operators, respectively. For the fourth-order Pade method, E is tridiagonal. For sixth-order methods, it is usually pentadiagonal. Compact-difference operators are thus of the form $C = M^{-1}E$ and are global (dense matrices).

An area of active research concerns stable boundary closures for compact-difference methods. In general, stencils are modified in the vicinity of boundaries, which results in some loss of formal accuracy. It is well known (Gustafsson, 1975) that, for a hyperbolic system of equations, a scheme of hth order closure can retain global formal accuracy of order $h + 1$ at best. In distinguishing between various schemes, we adopt the nomenclature of Carpenter *et al.* (1991). For example, 3,4–6–4,3 refers to a scheme that is of sixth-order accuracy at interior node points, fourth-order accuracy at nodes 1 and $N_z - 1$, and third-order accuracy at nodes 0 and N_z. Recently, Carpenter *et al.* (1991) have developed a 5,5–6–5,5 scheme which retains global sixth-order accuracy. It evaluates derivatives at the boundary points and at immediately adjacent points by fully explicit eight-point stencils. Among the schemes which we have tried and for which options exist in the DNS code are the 3–4–3 (Pade), 3,4–6–4,3 (Lele), and 5,5–6–5,5 (Carpenter *et al.*) schemes. The reader is referred to Lele (1990) and Carpenter *et al.* (1991) for details, including the coefficients of matrices M and E. These options exist for differentiation in both the streamwise and wall-normal directions. To date we have been unable to maintain numerical stability whenever fifth-order boundary closure is implemented in both the x and the z directions. Our most accurate results exploit the method of Carpenter *et al.* in the streamwise direction and the 3,4–6–4,3 method of Lele in the wall-normal direction.

All differentiation operators assume that grid points are equally spaced in computational space. Analytic functions, described in detail later, are used to map from computational space onto physical space, where the grid may be highly stretched. Metrics of the transformation are incorporated directly into the differentiation operators.

Time Advancement

To be practical, an explicit DNS algorithm must provide long-time temporal accuracy while requiring modest temporary storage. Unless excruciatingly well resolved in time, we believe that second-order schemes lack sufficient accuracy for DNS. Attempts to gain higher-order accuracy through multistep methods violate the latter practical constraint. An elegant compromise is afforded by the use of one of the family of third-order low-storage Runge–Kutta methods proposed by Williamson (1980). To implement the Runge–Kutta scheme, we cast the governing equations in the following form:

$$\frac{\partial \mathbf{Q}}{\partial t} = \mathbf{V},$$
$$\mathbf{V} \equiv -D_x^1 \mathbf{E} - D_\theta^0 \mathbf{F} - D_z^1 \mathbf{G} - \mathbf{H}. \tag{20}$$

Time advancement of the discrete version of (20) is accomplished in physical space. Such schemes are now in wide use, and so we omit details.

An important peripheral issue for DNS concerns the determination of a limit on the time step Δt, for which the time-advancement scheme remains stable, but which is not unnecessarily restrictive. For parameter values typical of high-speed boundary-layer flows, advection and viscous constraints on the time step are of the same order of magnitude. Moreover, if the flow is transitional, determination of an appropriate time step is complicated by localized large-scale velocity and temperature fluctuations. Consequently, we have chosen to estimate the stability limit dynamically so as to maintain the time step continually near its maximum allowable size. Specifically, we require

$$\max(\lim_1, \lim_2) \cdot \Delta t < sf,$$
$$\lim_1 = (\lim_a^2 + \lim_\mu^2)^{1/2}, \tag{21}$$
$$\lim_2 = (\lim_a^2 + \lim_\kappa^2)^{1/2},$$

where $0 < sf < 1$ is the stability limit safety factor (typically $sf = 0.95$), and where $\lim_a$, $\lim_\mu$, and $\lim_\kappa$ are limiting values obtained by independent consideration of the stability of model linear advection, viscous diffusion, and thermal diffusion equations, respectively. For example, to evaluate the advection limit, we consider the linear transport equation

$$q_t + (|u| + c)q_x + (|v| + c)q_y + (|w| + c)q_z = 0. \tag{22}$$

The coefficients u, v, and w are obtained from the instantaneously "frozen" velocity fields of the true problem. Similarly, the speed of sound $c = \sqrt{\gamma p/\rho}$ is computed from the "frozen" density and pressure of the true problem. The integration of (22) is stable provided

$$\Delta t \cdot \lim_a < 1,$$
$$\lim_a = \max_{ijk} \left[\frac{(|u| + c)_{ijk}}{cfl_x \Delta x_i} + \frac{(|v| + c)_{ijk}}{cfl_y \Delta y_j} + \frac{(|w| + c)_{ijk}}{cfl_z \Delta z_k} \right], \tag{23}$$

where $\Delta x_i \equiv x_i - x_{i-1}$, etc. The Courant–Friedrichs–Levy (CFL) limits cfl_x, cfl_y, and cfl_z depend upon both the method of temporal advancement and the eigenvalue spectrum of the discrete spatial operator exploited in the x, y, and z dimensions, respectively. Table 1 presents the stability limits of a variety of spatial operators for the one-dimensional linear advection (wave) equation integrated in time by a third-order Runge–Kutta (RK3) scheme. Some of these limits have been derived by rigorous

Table 1. Courant–Friedrichs–Levy (CFL) limit $|a(\Delta t/\Delta x)| < cfl$ for the scalar linear advection equation $q_t + aq_x = 0$.

Spatial operator	Stability limit cfl	Method of derivation
Compact fourth order	1.0	Empirical
Compact sixth order	$\sqrt{3}/2$	Analytical
Fourier spectral	$\sqrt{3}/\pi$	Analytical
Chebyshev spectral	$5(\sqrt{3}/\pi)$	Empirical

Table 2. Viscous stability limit $|\nu(\Delta t/\Delta x^2)| < \nu l$ for the scalar diffusion equation $q_t = \nu q_{xx}$.

Spatial operator	Stability limit νl	Method of derivation
Compact fourth order	2.51/3	Empirical
Compact sixth order	2.51/4	Empirical
Fourier spectral	$2.51/\pi^2$	Analytical
Chebyshev spectral	$2(2.51/\pi^2)$	Empirical

eigenvalue analyses and are so noted. Others have been established empirically by numerical experimentation with the time step, in which cases the scheme "blows up" whenever the time step exceeds the value given. For the Fourier spectral and finite-difference schemes, the stability limits are sharp. For the Chebyshev spectral scheme, the limit was harder to evaluate empirically because of the less explosive nature of the numerical instability; hence, we urge some caution in the use of the value presented.

Similarly, $\lim_\mu$ and $\lim_\kappa$ are defined by considering model diffusion equations of the form

$$q_t = \frac{\nu}{Re}\nabla^2 q, \qquad \nu \in \left\{\frac{\mu}{\rho}, \frac{\kappa}{\rho}\right\} \tag{24}$$

with the help of Table 2. The domain of absolute stability for third-order Runge–Kutta methods can be found in many references including Canuto *et al.* (1988). The factors of 2.51 and $\sqrt{3}$ which arise in Tables 2 and 1, respectively, pertain to the intercepts of the RK3 stability boundary with the real and imaginary axes, respectively. The stability of a diffusion problem is limited by the value -2.51 of the real-axis intercept, whereas the stability of an advection problem is limited by the values $\pm\sqrt{3}$ of the imaginary-axis intercepts. We conjecture that solutions of problems of mixed advection-diffusion type remain stable provided, say, the point $(-2.51 \cdot \lim_\mu, \sqrt{3} \cdot \lim_a)$ lies within the RK3 domain of absolute stability. Equation (21) is a convenient approximation to this criterion based on the fact that a half-ellipse through the real and imaginary intercepts lies entirely within this region.

The numerical stability of semidiscrete and fully discrete compact-difference schemes is subtle and, as mentioned previously, is currently an area of active research (Carpenter *et al.*, 1991). In general, what is true for scalar equations is not necessarily true for systems. Our method of estimating stability limits is somewhat heuristic, but it has proved a useful guideline in practical applications for a wide variety of numerical methods and over a wide range of parameter values. For the range of parameter values of the test cases in Section 5, approximately 1000 time steps per disturbance period suffice to maintain numerical stability.

Initial Condition

We obtain the initial ("basic") flow state $\mathbf{Q}^0$, which is assumed to be two-dimensional or axisymmetric, from the spectrally accurate boundary-layer (BL) code described in Pruett and Streett (1991) and Pruett (1993). Velocity and temperature profiles provided by this code are smooth nearly to machine precision. Either isothermal or adiabatic wall cases can be computed by the BL code. The present results assume that the wall is adiabatic. Because the boundary-layer equations neglect terms of order $1/Re_L$ and higher, a small residual remains when the boundary-layer solution is injected into the steady Navier–Stokes equations. Without special treatment, this numerical error introduces transients into the domain that may contaminate the Fourier analysis of the flow field. There are two philosophies for treating the initial residual. The governing equations can be integrated in time (relaxed) from the initial guess until the residual becomes arbitrarily small (in practice, on the order of machine zero). Unfortunately, for an explicit code, the computation of a clean steady state may require a greater computational effort than the computation of the perturbed flow of interest, since numerical errors may mimic slowly traveling physical waves. Alternately, small source terms can be subtracted from the governing equations to cancel the initial residual exactly (Erlebacher and Hussaini, 1990). To conserve computational resources, we adopt the latter method. For the parameter

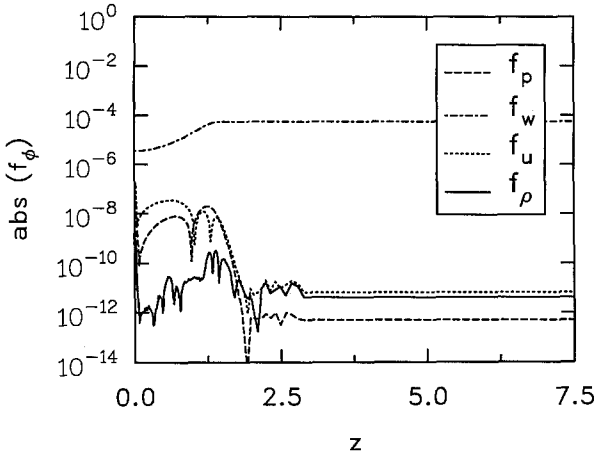

Figure 3. Components of source term $\mathbf{f} = [f_\rho, f_u, 0, f_w, f_p]^T$ subtracted from Navier–Stokes equations to cancel steady-state residual of base flow.

values of Cases 2 and 3 of Section 5, Figure 3 compares the magnitude of the components of the source term $\mathbf{f}$ that are subtracted from the continuity, u and w momentum, and pressure equations at the inflow station. The source term is small, but most significant, in the wall-normal momentum equation, where the slight transverse pressure gradient is neglected by the boundary-layer equations. An advantage of this approach is that it facilitates direct comparisons with LST and PSE analyses, both of which assume inherently that the base state is steady and simultaneously satisfies the governing equations.

For the presentation of results, it is often useful to display only the disturbance fields, which we denote by primes. That is, $\mathbf{Q}' \equiv \mathbf{Q} - \mathbf{Q}^0$ and similarly for individual components.

Boundary Conditions

As any practitioner of spatial DNS will acknowledge, the specification of boundary conditions for inflow–outflow problems is a delicate matter. The reader is referred to Nordstrom (1989) and Poinsot and Lele (1992) for detailed discussions of the issues involved. For Navier–Stokes calculations, all flow quantities can be specified at the inflow boundary. The prescription of the inflow condition depends upon the method by which disturbances are introduced into the flow. To date, spatial DNS calculations have introduced forcing either through a time-periodic inflow condition (e.g., originated, we believe, by DeSanto and Keller, (1962)) or through a time-periodic wall boundary condition (e.g., Kral, 1988; Thumm, 1991). For stability calculations, the difficulty with the latter method is that it is never known precisely what disturbances are generated. Indeed, in high-speed boundary-layer flows, it appears that multiple modes at the same frequency can he generated by periodic suction and blowing at the wall (Eissler and Bestek, 1993). Therefore, we favor the former approach. At the inflow boundary $x = x_{\text{in}}$, the flow is specified as the superposition of the steady two-dimensional or axisymmetric base flow and a temporally periodic fluctuation of frequency ω, amplitude ε, streamwise wave number α, and spanwise (azimuthal) wave number β as follows:

$$\mathbf{Q}(x_{\text{in}}, y, z, t) = \mathbf{Q}^0(x_{\text{in}}, z) + \varepsilon \exp[\imath(\alpha x_{\text{in}} + \beta y) - \omega t]\Psi(z) + \text{c.c.} \tag{25}$$

To minimize temporal transients, ε is ramped smoothly to its maximum value over an interval of time (typically one disturbance period). The disturbance structure, which is contained in the complex vector Ψ, is obtained either from spatial LST (Ng and Zang, 1993) or from PSE theory as in Chang *et al.* (1991). In either case the disturbance is normalized so that the maximum amplitude of the temperature fluctuation is unity. For high-speed flows, the disturbances derived from the parallel (LST) and nonparallel (PSE) theories are significantly different, as shown in Figure 4, and the disparity tends to increase with x and with Mach number. For developing (nonparallel) high-speed boundary-layer flows, the use of LST-derived forcing results in a significant inconsistency at the inflow boundary, which manifests itself in undesirable streamwise transients downstream of the inflow boundary.

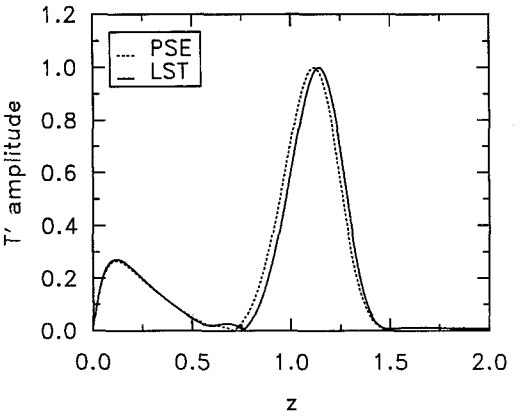

Figure 4. Amplitude of temperature component of linear disturbance at $Re_L = 700$ from parallel (LST) and nonparallel (PSE) theories.

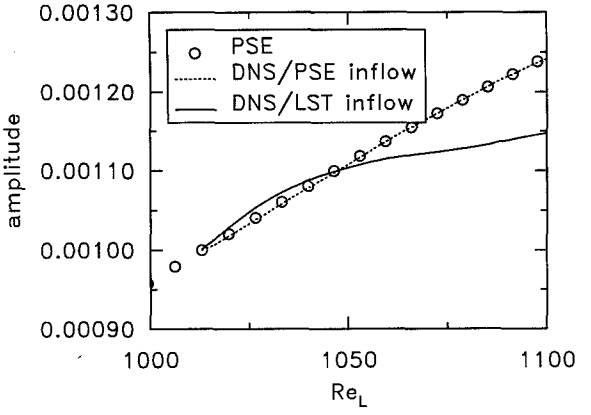

Figure 5. Transients downstream of inflow boundary for Case 4 of Section 5.

Moreover, if the amplitude of the disturbance is large enough, a weak Mach wave can be seen emanating from the inflow boundary near the critical layer. It is therefore important that nonparallel effects be considered. We have found PSE-derived forcing functions virtually to eliminate inflow inconsistencies, as shown in Figure 5, which presents the evolution of the temperature maximum in the region near the inflow boundary for Case 4 in Section 5. In contrast, the wandering of the temperature maximum away from the nearly constant-slope DNS/PSE curve for the DNS/LST case is symptomatic of the inconsistency between the parallel LST theory and the nonparallel DNS calculation.

For reference, the amplitudes of each of the five components Ψ of an oblique second-mode disturbance in a Mach 6.8 boundary-layer flow on a cone are shown in Figure 1, having been obtained from the nonparallel PSE method for parameter values which correspond to Case 4 in Section 5. Note the domination of the temperature and density components of the disturbance.

In the vicinity of the outflow boundary, we have found a buffer domain, proposed by Streett and Macaraeg (1989/90), to be effective in passing large-amplitude fluctuations with minimal reflection and upstream influence. Within the buffer region, the governing system of equations is gradually modified as follows:

1. Streamwise viscous terms are smoothly attenuated to zero to parabolize the governing system.
2. The base streamwise velocity profile is smoothly brought to that of a uniform flow at the velocity of the free stream to ensure that all characteristics lead out of the domain.
3. The source term **f** discussed previously is modified significantly in the buffer region to balance the changes to the basic flow.

With these changes, flow quantities along the outflow boundary can be extrapolated from the interior.

At the wall, the usual no-slip conditions are imposed on the velocities (except within the buffer region). Temperature is assumed to be fixed at its adiabatic value. (The rationale for the hybridization of the adiabatic and Dirichlet wall condition on temperature is addressed in an article by Pruett and Zang (1992) in a previous issue of this journal.) No condition is imposed on density; its value is determined directly from the governing equations at the wall. Pressure at the wall is derived from density and temperature via the equation of state.

At the far-field boundary ($z = z_{\max}$), we adapt the nonreflecting boundary conditions proposed by Thompson (1987), which are based in inviscid characteristic theory. Here, these are applied only to the disturbance field $\mathbf{U}' \equiv \mathbf{U} - \mathbf{U}^0$ in the following way. Adding and subtracting formally identical quantities from the right-hand side of (20), we obtain

$$\frac{\partial \mathbf{Q}}{\partial t} = \mathbf{V} - \frac{\partial \mathbf{G}'}{\partial z} + \frac{\partial \tilde{\mathbf{G}}'}{\partial z}, \tag{26}$$

where

$$\frac{\partial \mathbf{G}'}{\partial z} \equiv \frac{\partial \mathbf{G}}{\partial \mathbf{U}} \frac{\partial \mathbf{U}'}{\partial z}. \tag{27}$$

Recognizing that

$$\frac{\partial \mathbf{Q}}{\partial t} = \frac{\partial \mathbf{Q}}{\partial \mathbf{U}} \frac{\partial \mathbf{U}}{\partial t}$$

and exploiting the notation $A = \partial \mathbf{Q}/\partial \mathbf{U}$ and $B = \partial \mathbf{G}/\partial \mathbf{U}$, we temporarily recast (26) in terms of $\mathbf{U}$ as follows:

$$\frac{\partial \mathbf{U}}{\partial t} = A^{-1}\mathbf{V} - (S - \tilde{S})\frac{\partial \mathbf{U}'}{\partial z}, \tag{28}$$

where $S \equiv A^{-1}B$, and $\tilde{S}$ has yet to be defined. Matrix S is then diagonalized by the similarity transformation $S = P\Lambda P^{-1}$, where Λ is the diagonal matrix with eigenvalues $\lambda_m \in \{w - c, w, w, w, w + c\}$ in the order shown. Positive and negative eigenvalues correspond to outbound and inbound characteristics, respectively. Now let $\tilde{S} = P\tilde{\Lambda}P^{-1}$, where $\tilde{\Lambda}$ is the diagonal matrix with eigenvalues $\tilde{\lambda}_m = \max(\lambda_m, 0)$. Writing (28) once again in terms of $\mathbf{Q}$, we obtain our working form

$$\frac{\partial \mathbf{Q}}{\partial t} = \mathbf{V} - AP[\Lambda - \tilde{\Lambda}]P^{-1}\left[\frac{\partial \mathbf{U}}{\partial z} - \frac{\partial \mathbf{U}^0}{\partial z}\right]. \tag{29}$$

Note that if $\mathbf{U} = \mathbf{U}^0$, or if all eigenvalues of Λ are nonnegative, then there is no change to the right-hand side vector $\mathbf{V}$. If, however, there are disturbances traveling inbound at the far-field boundary, their time derivatives are set to zero on the boundary.

Mappings

As shown in Figure 1, the eigenfunction of a second-mode disturbance in a high-speed boundary-layer flow has a double structure in which the temperature component is sharply peaked near the wall and the critical layer. Consequently, accuracy and resolution considerations necessitate that grid points be clustered in both regions of sharp gradients. For this purpose, we use a highly tuned mapping from the computational space to the physical space. The mapping is adapted from Erlebacher and Hussaini (1990) and combines gradual exponential stretching away from the wall with clustering in the vicinity of the critical layer. In computational space, for $k = 0, 1, \ldots, N_z$,

$$\xi_k = \begin{cases} -1 + \dfrac{2k}{N_z}, & \text{compact difference,} \\ \cos\left(\dfrac{k\pi}{N_z}\right), & \text{Chebyshev spectral.} \end{cases} \tag{30}$$

For the compact-difference schemes, note that grid points are equally spaced in computational space. There are five parameters for the mapping: $z_{\max}$, $z_{1/2}$, z_0, Δz, and τ. The following transcendental equation maps the interval $[-1, +1]$ in computational space onto itself and performs a clustering of grid points of strength τ and width Δz about the point z_0:

$$\zeta + \tau \tanh\left[\frac{\zeta - \zeta_0}{\Delta\zeta}\right] = \frac{\xi - \xi_0}{\Delta\xi}, \qquad -1 \le \xi \le +1. \tag{31}$$

The subsequent exponential transformation below maps the computational interval $[-1, +1]$ onto the physical interval $[0, z_{\max}]$:

$$z(\zeta) = z_{\max}\left[\frac{a^{(\zeta+1)} - 1}{a^2 - 1}\right], \qquad -1 \le \zeta \le +1,$$
$$a = \frac{z_{\max} + \sqrt{z_{\max}^2 - 4z_{1/2}(z_{\max} - z_{1/2})}}{2z_{1/2}}. \tag{32}$$

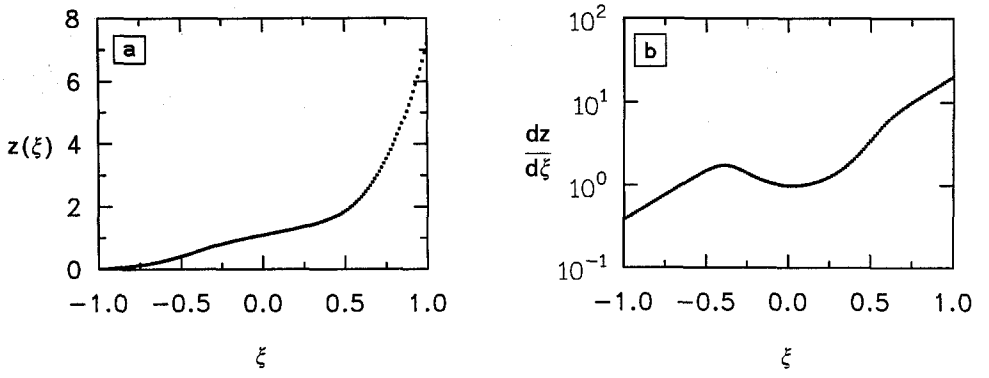

Figure 6. Wall-normal (a) mapping and (b) associated metric.

The four remaining unknown quantities in (31) are determined by requiring

$$z(\zeta_0) = z_0, \qquad \Delta\zeta = \frac{d\zeta}{dz}\cdot\Delta z, \qquad \zeta(-1) = -1, \qquad \zeta(+1) = +1. \tag{33}$$

If $\tau = 0$, there is no clustering about z_0, in which case exactly half of the grid points lie between the wall and $z_{1/2}$. We find (32) to be superior to the bilinear fractional transformation used originally by Erlebacher and Hussaini (1990), which stretches too fast in the far field. Figure 6 shows the grid-point distribution and metric for the parameter values of Mach 4.5 in Cases 2 and 3 in Section 5. In practice, we tune the number of grid points and mapping parameters by use of the temporal DNS code of Pruett and Zang (1992). More specifically, we adjust the resolution and mapping parameters until we are able to recover local (global) disturbance growth rates from the DNS that are in four (six) place agreement with eigenvalues obtained from temporal LST.

Similarly, a streamwise mapping can be used to concentrate points downstream where nonlinear interactions lead to a broadening of the spectrum in wave space. For this paper, however, all results were obtained with grid points equally spaced in x.

In spatial DNS the boundary layer thickens as x increases. Eventually, the mapping described above will become detuned, and the far-field boundary at $z_{\max}$ will pinch the flow unless the physical domain grows in wall-normal extent approximately as fast as the boundary layer. Motivated by boundary-layer theory, we define $z = \eta f(x)$ where $f(x)$ is a smooth function which grows like the boundary layer. For laminar flow, an appropriate choice is $f(x) = \sqrt{x/x_0}$. An option is provided in the DNS code to fix the far-field extent of either z or η. In the latter case the physical grid is nonorthogonal and streamwise and wall-normal derivatives are modified via the chain rule as follows:

$$\begin{aligned} \frac{\partial}{\partial x} &\to \frac{\partial}{\partial x} - \eta\frac{f'(x)}{f(x)}\frac{\partial}{\partial \eta}, \\ \frac{\partial}{\partial z} &\to \frac{1}{f(x)}\frac{\partial}{\partial \eta}. \end{aligned} \tag{34}$$

With the exception of the first case in Section 5, the results presented below were obtained with the growing-domain option.

Filtering

From the work of Trefethen (1982), Vichnevetsky (1986), and Poinsot and Lele (1992), it is clear that all finite-difference schemes reflect some energy at outflow boundaries. Typically the reflection coefficient (i.e., the ratio of incident to reflected energy) behaves like $(\alpha\Delta x)^h$, where h is the order of the scheme and α is the disturbance wave number. Moreover, numerical reflections arise even if the physical boundary conditions imposed are perfectly nonreflecting. Regardless of the order of the

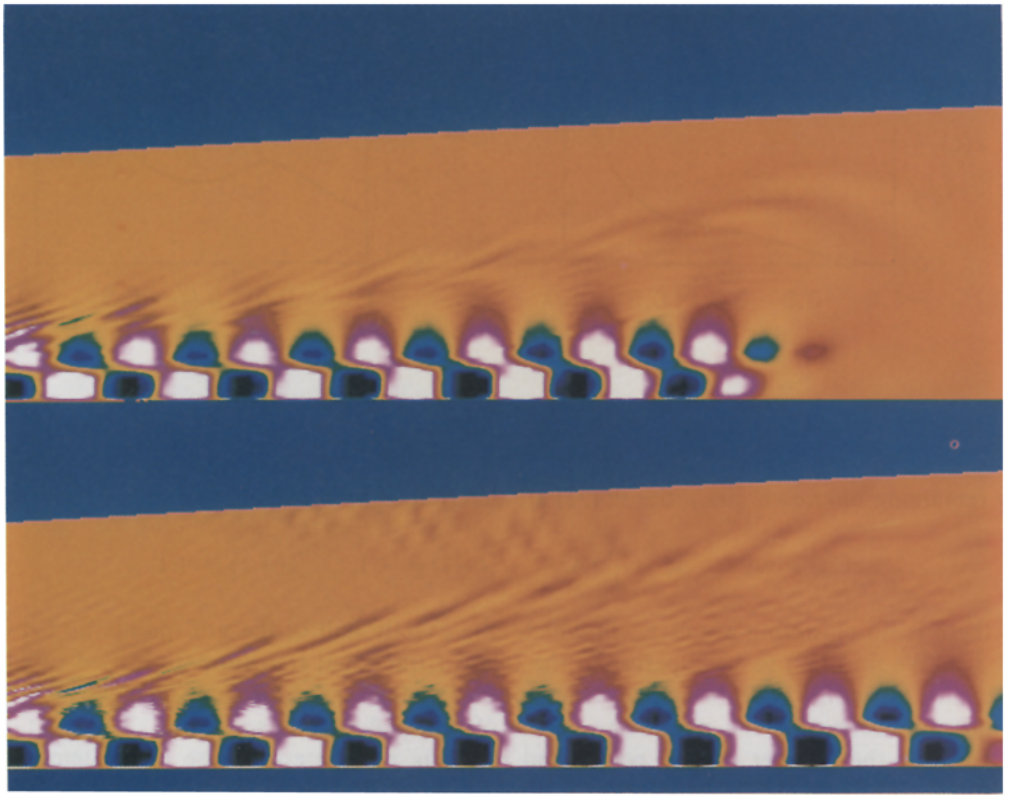

Figure 7. Two-point oscillations and spurious physical waves in disturbance pressure p' in absence of filtering. Two-dimensional Mach 4.5 flat-plate boundary-layer flow with parameter values similar to Case 2 of Section 5. Streamwise extent limited to nine disturbance wavelengths. Wall-normal extent $0 \leq \eta \leq 7.5$. Upper and lower photographs, respectively, show instants in time before and after exit of leading wavefront from computational domain.

scheme, energy at the "sawtooth" wavelength ($\alpha \Delta x = \pi$) is usually totally reflected. As shown by Trefethen (1982) and Vichnevetsky (1986), reflected energy travels upstream as a wave packet at the group velocity V_g, which depends on the spatial discretization scheme. As mentioned by Poinsot and Lele (1992), for the one-dimensional Euler equation, the group velocities of the fourth-order and sixth-order central compact-difference schemes are $3(|u| + c)$ and $14(|u| + c)/3$, respectively. Once the wave packet encounters the Dirichlet inflow condition, which is numerically reflecting to all wavelengths, it reforms and travels downstream as a spurious physical disturbance. For the sixth-order compact-difference scheme, this entire phenomenon masquerades as an apparent coupling between the outflow and inflow boundaries, whereby spurious physical oscillations emanate from the inflow boundary shortly following the exit of the leading wavefront from the outflow boundary, as shown by the flow-visualization sequence in Figure 7. The photograph shows the instantaneous disturbance pressure p' at two different times in a simulation of a two-dimensional Mach 4.5 flat-plate boundary-layer flow. The parameter values are similar to those of Case 2 of Section 5. However, the corrective filtering described below has not been implemented, and, for clarity, the domain is foreshortened to a length of nine disturbance wavelengths in streamwise extent. The upper photograph shows p' prior to the arrival of the leading wavefront at the outflow plane. Two-point oscillations, predominantly in the wall-normal direction, are clearly visible just outside the boundary layer. The lower photograph, with precisely the same color scale, shows p' several periods after the exit of the leading wavefront from the domain. Note the appearance of spurious physical waves along the upper boundary, the ultimate result of a numerical double reflection off the outflow and inflow boundaries.

One of several possible solutions, including upwind biasing, is through filtering, which we prefer for its simplicity and efficiency. Outside the boundary layer, the physical viscosity has a vanishingly small

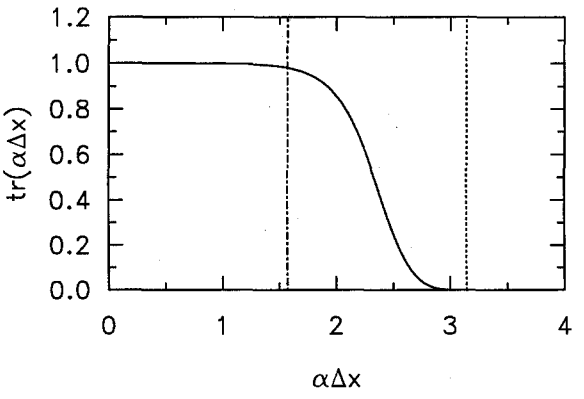

Figure 8. Transfer function tr($\alpha\Delta x$) for sixth-order compact-difference filter.

effect; without some added numerical dissipation, the central-difference approximations result in odd–even decoupling that introduces energy at the troublesome "sawtooth" wavelength. The trick is to keep energy at this wavelength from crossing the outflow boundary. Here, minimal damping is imposed by periodically applying a low-pass sixth-order compact-difference filter (Lele, 1990) to the solution. Typically we apply the filter every few time steps, in which case the additional computational effort is insignificant when amortized over, say, nine Runge–Kutta stages. Moreover, we find it necessary to apply the filter only in the wall-normal direction.

Lele's sixth-order filter has two free parameters. For the values we have chosen, the formal truncation error for filtering a function $f(x)$ is $\frac{1}{640}(\Delta x)^6 f^{(6)}$, and the transfer function is shown in Figure 8. Two-point oscillations (shown by the vertical dotted line) are completely eliminated by the filter, whereas oscillations of twice that wavelength (shown by the vertical dashed-dotted line) and longer are virtually undamped. In practice, the filter incorporates third-order boundary closure (Lele, 1990), which reduces the global accuracy to fourth order, as does the boundary closure of the 3,4–6–4,3 compact-difference scheme. The filter parameters and frequencies in current use are in no sense optimal, and it may well be possible to reduce the modest computational effort still further by less frequent filtering.

An additional subtlety arises when implementing the filter in the context of a total variable formulation of the governing equations (rather than a disturbance variable formulation). Over many applications, filtering effects gradual evolution of the base state. For example, for a simulation similar to that of Case 4 in Section 5, but with a foreshortened domain (one-sixth the streamwise extent of Case 4) and no imposed disturbance ($\varepsilon = 0.0$), the base density changes approximately 0.01% in 1.4 flow-through times when filtering is applied every third time step. This presents two problems. First, because of the extreme sensitivity of the stability of the flow to changes in the base state, unintended evolution of the base state may affect hydrodynamic stability. Second, when the basic state is subtracted from the total-flow variables for purposes of flow visualization, the disturbance fields, whose velocity components may be, say, of order 10^{-6}, are contaminated. The difficulty is corrected by incorporating an additional steady source term $\mathbf{f}_1$, to be defined shortly, into the right-hand side of the governing equations. For simplicity, in the context of a first-order (forward Euler) time-integration scheme, the filtering algorithm can be summarized as follows:

For $l = 0, 1, 2, \ldots$

$$\begin{aligned} &\mathbf{q}^{l+1} = \tilde{\mathbf{q}}^l + \Delta t \cdot [\mathbf{v}(\tilde{\mathbf{q}}^l) - \mathbf{f} - \mathbf{f}_1] \\ &\tilde{\mathbf{q}}^{l+1} = F\mathbf{q}^{l+1} \end{aligned} \tag{35}$$

where $\mathbf{q}$ and $\mathbf{v}$ denote the discrete representations of $\mathbf{Q}$ and $\mathbf{V}$, respectively, a tilde denotes a filtered quantity, F is the discrete filter operator, and l is the time-level index. In practice, $P\tilde{\mathbf{q}}^l = H\mathbf{q}^l$, where P and H are pentadiagonal and heptadiagonal matrices, respectively, whereby $F = P^{-1}H$. Recognizing

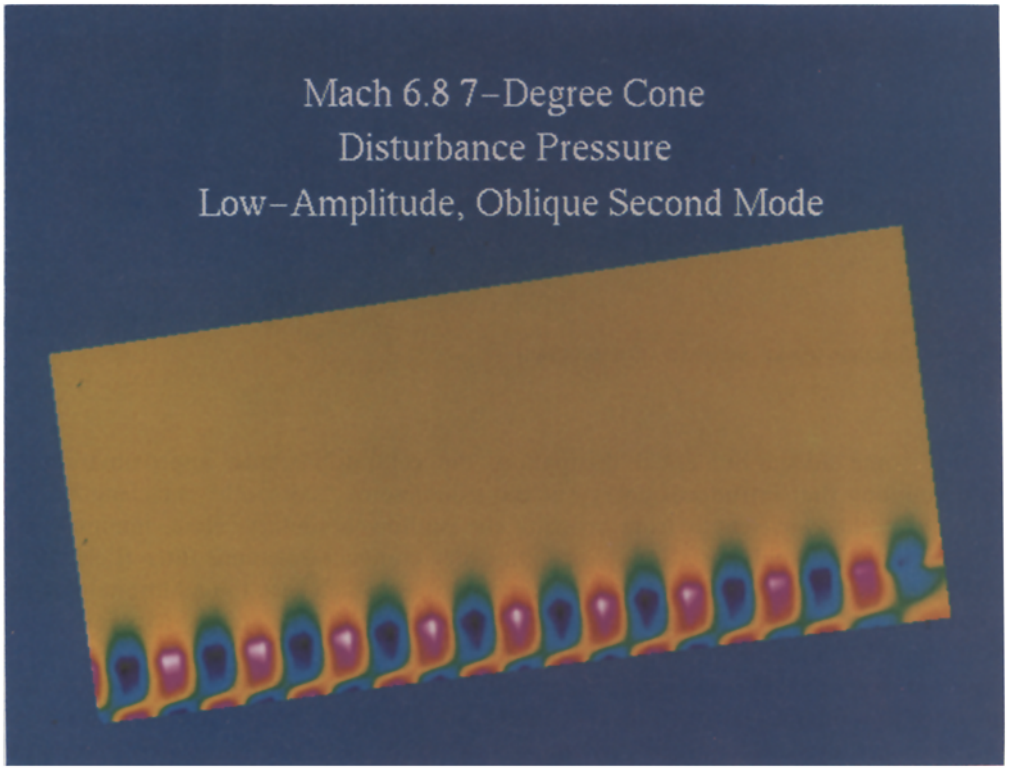

Figure 9. Instantaneous disturbance pressure p' at time of 53 periods of oscillation of fundamental for Case 4 of Section 5. For clarity, computational domain truncated in streamwise extent to $1436 \leq Re_L \leq 1536$. (Buffer domain shown.) Wall-normal extent $0 \leq \eta \leq 7.5$. Results shown in "peak" plane $\theta = 0$. Colors depict contour levels between -3×10^{-6} and 3×10^{-6}.

that (by definition) $\mathbf{v}(\tilde{\mathbf{q}}^0) - \mathbf{f} = \mathbf{0}$ identically, the reader can readily show from (35) that if $l = 0$ and $\mathbf{f}_1 \equiv [(F - I)/\Delta t]\mathbf{q}^0$, then $\mathbf{q}^1 = \mathbf{q}^0$. That is, formally the base state is preserved over the first and all subsequent time steps in the absence of forced disturbances. In practice, the additional source term $\mathbf{f}_1$ is "turned on" only immediately prior to filtering operations, in which case the filtered basic state remains constant over time nearly to machine precision.

Figure 9 is presented to illustrate the beneficial effects on the solution of the filtering algorithm described above, including the adjustment to prevent unintentional evolution of the base state. It portrays the instantaneous disturbance pressure p' obtained from Case 4 of Section 5. For clarity, however, only the final ten disturbance wavelengths of the computational domain (including the buffer domain) are shown. The time corresponds to 53 periods of oscillation of the disturbance. We note that the maximum amplitude of p' is quite small, in our normalization, more than two orders of magnitude below that of T', whose amplitude at the inflow boundary is $\varepsilon = 0.001$. In contrast to Figure 7, two-point oscillations have been completely damped, thereby eliminating detectable boundary reflections and spurious physical waves, without detriment to the evolution of the instability wave.

4. Algorithm Details

In algorithm design there is frequently a tradeoff between computational effort and storage requirements, as is the case here. For a fully explicit scheme, storage requirements are modest, and the overriding consideration is to minimize the computational work per time step. We discuss very briefly several considerations which contribute to the efficiency and simplicity of the algorithm.

For the three-dimensional compressible Navier–Stokes equations, the minimum number of partial derivative computations required by an explicit algorithm to evaluate $\mathbf{V}$ is 27: 9 for the rate-of-deformation tensor, 3 for the heat flux components, and the remaining 15 for the components of the

flux vectors **E**, **F**, and **G**. Both our conservative (energy equation) and nonconservative (pressure equation) formulations require only the minimum number of 27 partial derivative evaluations. Specifically, partial derivative evaluations are implemented through calls to a subroutine PARTIAL whose arguments specify:

1. The direction of the derivative.
2. Whether or not to include certain terms which arise from nonzero Christoffel symbols as in the distinction between $D_z^0 u$ and $D_z^1 u$ in (3).
3. If spanwise (azimuthal) symmetry is enforced, whether or not the function is even or odd.

Parameters passed to PARTIAL also specify the difference schemes for each coordinate direction. By this construction we have a wide range of possible options without complicating the core subroutine that evaluates the right-hand side vector **V**. The present algorithm uses (we believe) the minimum storage possible given the minimum work constraint previously discussed. The conservative (energy) formulation of the governing equations requires 18 storage arrays of approximate size $N_x \times N_\theta \times N_z$: 6 for the primitive variables **U** and the viscosity, 5 for storing components of the right-hand side vector **V**, 6 for temporary use in the evaluation of **V**, and 1 for partial derivative evaluations. A significant advantage of the nonconservative (pressure) formulation is that only 16 storage arrays are required. Since the energy equation and pressure equation formulations yield essentially identical results, we favor the pressure formulation for computational efficiency. For both formulations, one additional array is required if the growing-domain option is invoked.

Finally, for computational efficiency, innermost loops typically range over all $(N_x + 1) \times (N_\theta + 1)$ grid points in a surface of constant k, ensuring nearly optimal speed-up on vector processors. For directionally dependent calculations such as FFT evaluations and the solution of tridiagonal systems, the inner computational loop ranges over the number of independent transforms or right-hand sides. On single processors of the Cray Y-MP and the Cray C90, the present algorithm performs at greater than 150 megaflops and 415 megaflops, respectively. In recent calculations on the C90, the algorithm has been assessed at 5.6×10^{-6} seconds per gridpoint per (full) time step.

5. Validation

For comparisons with DNS results, we rely on compressible LST (Mack, 1984; Ng and Zang, 1993) and on results obtained by the compressible PSE method of Chang *et al.* (1991). The reader is referred to these authors for details. Briefly, in classical LST, an eigenvalue problem results from certain assumptions about the basic flow and the wave-like nature of the disturbances. Because of the assumptions, the results of LST are strictly valid only for low-amplitude (linear) disturbances in parallel base flows. Our LST results were obtained from the spectrally accurate spatial linear stability code of Ng and Zang (1993).

The PSE approach uses a traveling wave *ansatz* similar to LST, except that the disturbance shape function (Ψ in (25)) is allowed to vary in both the wall-normal and the streamwise directions. Rapid oscillation of the wave is incorporated into the exponential part of the wave *ansatz*, whereby the shape function evolves in x on a scale much longer than a wavelength. The governing equations thereby reduce to a set of PDEs for the shape function only. The PSE method becomes approximate, rather than exact, when these PDEs are parabolized to facilitate a marching solution. Provided the instabilities are of convective nature, as they are for most high-speed boundary-layer flows, the parabolization approximation is quite reasonable. For nonlinear problems, the disturbances are expressed as Fourier series in the frequency domain. The equations for each Fourier mode are independent except through inhomogeneous terms which arise due to nonlinear mode interactions. Therefore, the PSE method can treat both nonparallel and moderately nonlinear effects.

The comparison of DNS results with those obtained by LST and PSE requires the Fourier decomposition of the DNS data in time and in the azimuthal (spanwise) dimension. The resulting modes are identified with ordered pairs (m_ω, m_β), where the integers m_ω and m_β label the harmonics in Fourier space with respect to the temporal frequency ω and the azimuthal wave number β, respectively. For example, the fundamental mode is labeled (1, 0) if two-dimensional or (1, 1) if oblique.

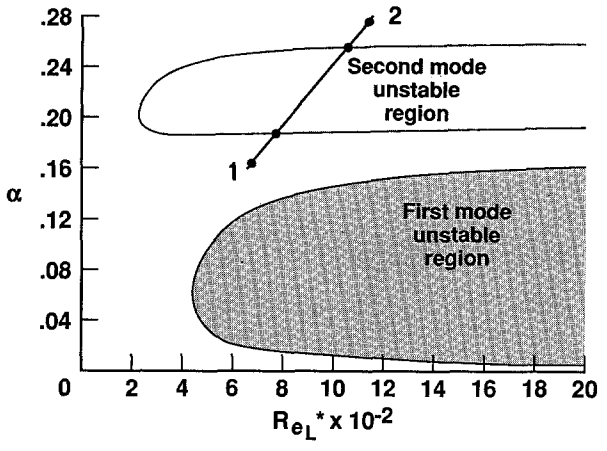

Figure 10. First- and second-mode unstable regions for Mach 4.5 flat-plate boundary layer (after Mack, 1984).

We present four validation cases. The first three consider two-dimensional second-model disturbances in Mach 4.5 flow along a flat plat. Of these three, the first two examine the evolution of low-amplitude disturbances in parallel and nonparallel boundary-layer flows, respectively. In the third test case, forcing is of large amplitude and harmonics generated by nonlinear interactions attain significant amplitudes. The final test case considers the evolution of a pair of symmetric oblique (helical) second-mode disturbances in a Mach 6.8 boundary-layer flow along a cone.

As a point of reference for the flat-plate cases, we include Figure 10 (adapted from Mack, 1984), which shows distinct regions of instability for first- and second-mode disturbances in a Mach 4.5 planar boundary-layer flow. However, we caution against attempts at exact comparisons for these reasons: Mack's diagram is derived from temporal, rather than spatial, LST; LST inherently assumes locally parallel flow; and Mack uses a slightly different formula for viscosity.

Case 1: Flat Plate, Mach 4.5 Parallel Flow, Two-Dimensional Linear Disturbance. Our primary purpose here is to evaluate the resolution required in the streamwise direction to capture accurately the evolution of a monochromatic disturbance. Figure 11 compares the computed (DNS) and theoretical (LST) maximum amplitude of the temperature fluctuation for a disturbance of dimensionless frequency $F = \omega^* L^*/(u_e^* Re_L) = 2.29 \times 10^{-4}$, $Re_L = 955.67$, and amplitude $\varepsilon \ll 1$ in flat-plate adiabatic-wall flow with $M_e = 4.5$ and $T_e^* = 61.11$ K. These parameter values define a slightly damped second-mode disturbance that corresponds to a point just beyond the upper branch neutral curve in Figure 10. For the DNS, the computational domain spans eight wavelengths in streamwise extent (based on parallel, linear theory). The amplitude maxima versus x are determined by Fourier time-series analysis over the interval from 13 to 14 periods of oscillation of the disturbance, after the leading wavefront has exited the domain. DNS results are shown for the 5,5–6–5,5 scheme at streamwise resolutions of

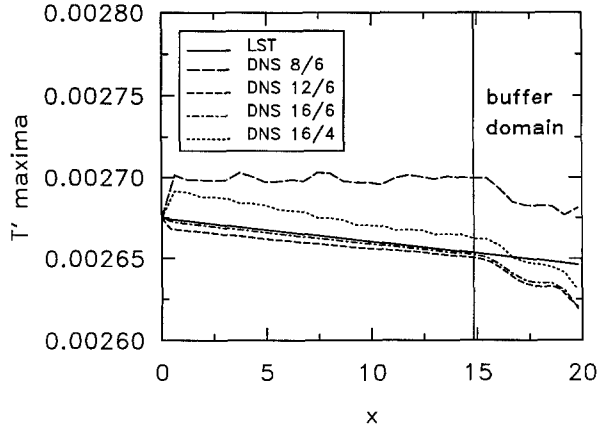

Figure 11. Case 1: DNS and LST results for linear stability problem. In the legend "DNS 16/6," for example, denotes results obtained from spatial DNS by 6th-order differencing and 16 gridpoints per wavelength in the streamwise direction.

8, 12, and 16 grid points per disturbance, wavelength and for the 3–4–3 scheme with 16 grid points per wavelength. (In the legend for Figure 11, the first and second integers refer to the number of grid points per wavelength and the order of the scheme, respectively.) In all cases, wall-normal differencing is accomplished by the 3,4–6–4,3 compact-difference scheme with $N_z = 144$. For direct comparison with LST, the base flow is parallel (i.e., $u = u(z)$, $T = T(z)$, and $w = 0$), in which case the forcing terms analogous to Figure 3 are considerably larger than in the developing (nonparallel) flow case. For the fourth-order scheme and for the sixth-order scheme with fewer than 12 points per wavelength, significant oscillations are seen in the maxima. For the sixth-order scheme, the eigenvalue extracted from the DNS is correct to about three and four places for 12- and 16-point resolutions, respectively, except in the immediate vicinity of the inflow boundary where there is a very slight streamwise transient. The resolution needed for accurate results is about twice the six to eight points per wavelength we would have naively anticipated. For nonlinear problems, these results suggest that it is desirable to resolve the shortest wavelengths (highest harmonics) with at least 12 points per wavelength.

Figure 11 also offers reasonable validation of the buffer-domain outflow condition; no appreciable influence is evident on the decay rate of the instability wave upstream of the edge of the buffer domain (shown by the vertical line).

Case 2: Flat Plate, Mach 4.5 Nonparallel Flow, Two-Dimensional Linear Disturbance. Case 2 corresponds approximately to the ray that extends through points 1 and 2 in Figure 10 (Mack, 1984). In this case an evolving (nonparallel) Mach 4.5 flat-plate boundary-layer flow with the same flow parameters as before is forced at a dimensionless frequency $F = 2.2 \times 10^{-4}$. We note that, for Cases 1–3, the ratio δ^*/L^* is constant along the plate with the value 10.46. For the DNS, the inflow and outflow boundaries correspond to $Re_x = 0.49 \times 10^6$ ($Re_L = 700$) and $Re_x = 1.404 \times 10^6$ ($Re_L = 1185.3$), respectively. Over this range of Reynolds numbers, the selected frequency excites a second-mode disturbance. Relative to Figure 10, the computational domain is 36 wavelengths long (based on linear, nonparallel theory at x_{in}) and spans roughly from point 1 (just prior to the lower branch neutral point) to point 2 (somewhat beyond the upper branch neutral point). For the DNS, $N_z = 144$ and $z_{max} = 7.5$. Grid-point clustering and stretching is such that 75% of all points fall in the region bounded by the wall and $z = 1.4$. The buffer region spans the last 5% of the domain in x (i.e., the last 1.8 wavelengths). For comparison with LST, a small amplitude of $\varepsilon = 0.001$ is used for the DNS calculation to render insignificant the nonlinear terms of second order or higher in ε. The present results were obtained for $N_x = 576$, with points equally spaced in x, and can be considered very well resolved at 16 grid points per wavelength.

The PSE and DNS calculations both proceed from identical disturbance states. However, their respective base states were derived independently, that of the PSE calculation being obtained by finite-difference techniques. The amplitude distributions of the disturbance components imposed at the inflow station can be found in Figure 2 of Pruett and Chang (1993). Because the PSE calculation is linear, amplitude is arbitrary. For the comparison, the amplitudes of the PSE and DNS density fluctuations are equated at the inflow station, and all other disturbance quantities are scaled proportionately. Since the PSE computation is performed in Fourier space, the solution provides the contents of individual modes by default. To extract the temporal Fourier harmonics from the DNS data, we perform a time-series analysis analogous to hot-wire anemometry in physical experiments. The flow field is sampled over time at selected grid points (usually a substantial subset of the computational grid) and is subsequently Fourier analyzed for its harmonic content. Figure 12 presents the amplitude envelope of the density component of the fundamental mode versus η, obtained from 32 samples that span the one-period interval between periods 42 and 43. Because the phase velocity of the second-mode disturbance is about 90% of the edge velocity, by period 42 the leading wavefront has exited the outflow boundary and the flow has settled into a quasi-steady periodic state. Individual profiles in Figure 12(a) correspond to different streamwise locations, equally spaced between the inflow boundary and a point 32 wavelengths downstream (ahead of the beginning of the buffer region). For clarity, these profiles are each staggered by a factor of 2 on the logarithmic plot; hence, their maxima are relative, not absolute. Figure 12(b) graphs the density maxima obtained from Figure 12(a) versus the streamwise coordinate x. In Figure 13 the density maxima and the maxima of other

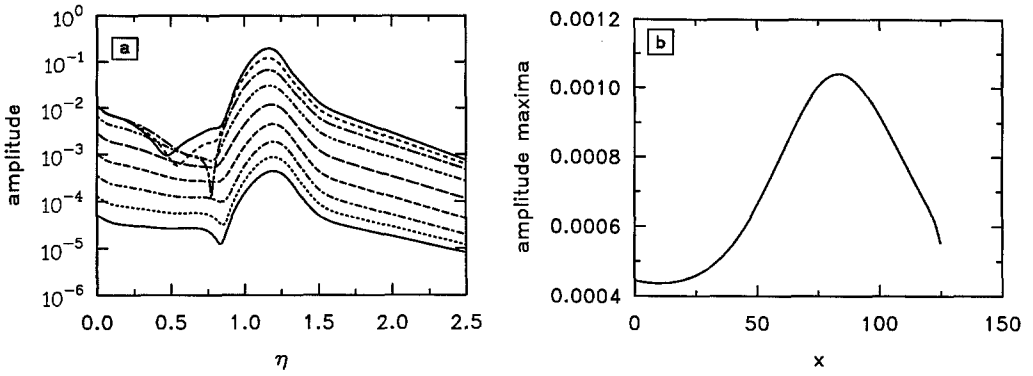

Figure 12. Case 2: Density fluctuation (a) amplitude distribution and (b) amplitude maxima for DNS.

flow quantities obtained in analogous fashion are plotted versus Re_L (rather than versus x) and are compared with the PSE results. For clarity, only every eighth DNS value is plotted. As shown in Figure 13, the agreement between the PSE and DNS results is excellent. The rapid divergence of the DNS and PSE results near the outflow boundary is attributed to the nonphysical damping of the instability wave as it traverses the buffer region and should be disregarded. From Figure 13, it can be observed that, in a nonparallel flow, maxima (or minima) of the various components of the disturbance do not necessarily occur at the same streamwise locations. Hence, neutral points and growth rates are nonuniquely defined. Based on the temperature component of the disturbance, the lower and upper branch neutral points occur at approximately $Re_L = 740$ and $Re_L = 1050$, respectively, in surprisingly good agreement with Figure 10.

Although Figure 13 shows good agreement at maxima, it provides no information about the disturbance structure. In Figure 14 we compare the velocity and density profiles of the PSE and DNS calculations at the station $Re_L = 1046$ near the location of the global maximum of the temperature fluctuation. For comparison of the disturbance structure, we scale the DNS and PSE results so that their respective density maxima are unity. Before rescaling, the respective maxima differ by less than 0.5%. For clarity, only every third DNS value (denoted by symbols) is shown in the figure. Despite the complex nature of the disturbance structure, the agreement is excellent. Moreover, this agreement confirms that the rapid change in the disturbance structure at the three stations that are farthest downstream in Figure 12(a) is a physical change and not the result of a computational anomaly.

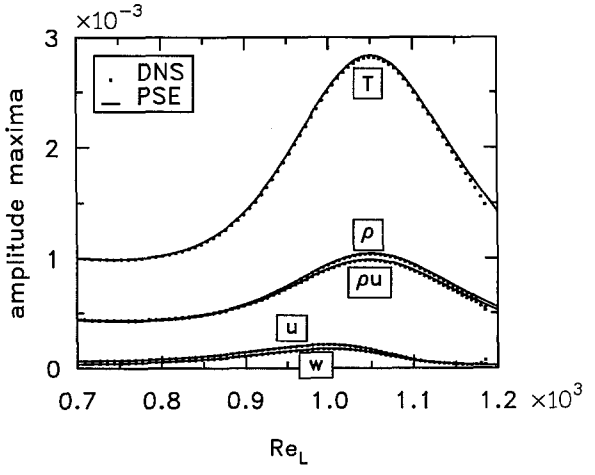

Figure 13. Case 2: PSE and DNS disturbance amplitude maxima versus Re_L.

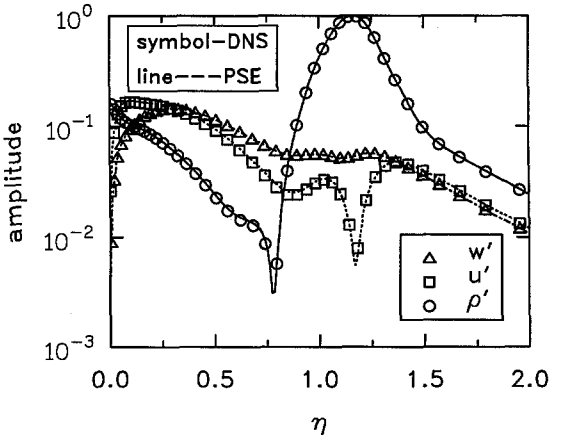

Figure 14. Case 2: Disturbance structure at $Re_L = 1046$.

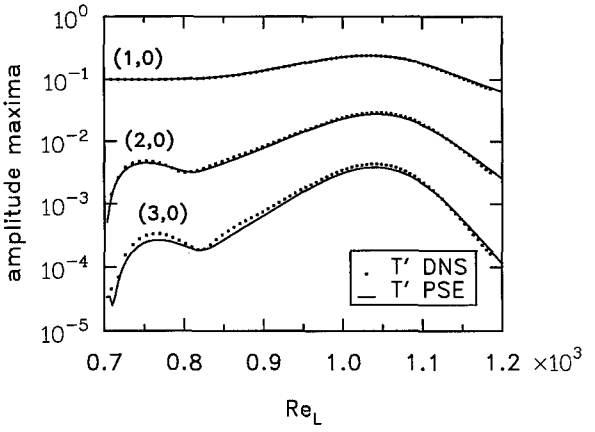

Figure 15. Case 3: Amplitude maxima of fundamental of temperature fluctuation and first two harmonics.

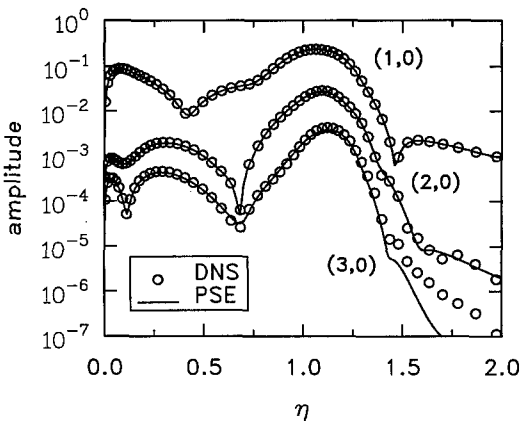

Figure 16. Case 3: Structures of fundamental and first two harmonics of temperature fluctuation at $Re_L = 1050$.

Case 3: Flat Plate, Mach 4.5 Nonparallel Flow, Two-Dimensional Nonlinear Disturbance. With regard to parameter values, this case is identical to the case above, except that the forcing amplitude is quite large at $\varepsilon = 0.1$. At this level of forcing, temperature fluctuations will grow in amplitude to a value that is 25% of the edge temperature of the base flow. For the DNS calculation, wall-normal resolution remains as before; however, 32 grid points per primary disturbance wavelength are used for a total of 1153 points in x. Based on the resolution criterion established for the linear case, the fundamental and its first harmonic are well resolved. The second harmonic, however, is somewhat underresolved. Higher harmonics, which contain very little energy, are unresolved.

Figure 15 compares the PSE and DNS results with regard to the streamwise evolution of the maxima of the temperature component of the fundamental and its first two harmonics. For the DNS, the Fourier analysis is performed on 32 time samples that span the interval between periods 48 and 49. The methods agree well qualitatively and quantitatively; however, greater disagreement occurs as the index of the harmonic increases. At the streamwise location of maximum disturbance amplitude, the PSE and DNS results differ by 0.15%, 6%, and 12%, respectively, for the fundamental (1, 0), the first harmonic (2, 0), and the second harmonic (3, 0). (Recall that, because the present calculation is two-dimensional, $m_\beta = 0$.)

A further comparison is shown in Figure 16, in which the PSE and DNS predictions of the structure of the temperature component of the fundamental and its first two harmonics are compared. In contrast to the (linear-amplitude) results presented in Figure 14, the present (nonlinear-amplitude) results have not been rescaled and are presented on a logarithmic scale so that all three modes can be shown with clarity. Between the wall and the critical layer, both methods produce similar amplitude distributions. Outside the boundary layer, there is divergence between the PSE and DNS results in the asymptotic rate of decay of the second harmonic. There are any number of possible physical and/or numerical reasons for this discrepancy. Among these are the differences between PSE and DNS in the imposition of far-field boundary conditions. In the PSE approach Dirichlet conditions are imposed on the disturbance in Fourier space at very large η (typically $\eta \approx 50$). Details of the imposition of boundary conditions for the PSE method can be found in Chang *et al.* (1991). In the DNS, inviscid characteristic conditions (described previously) are imposed in physical space along the far-field boundary $\eta = 7.5$. However, we remind the reader that the logarithmic scale of Figure 16 exaggerates these differences, which are of order 10^{-6} relative to the base state, and it is beyond our current intentions to ferret out the sources of errors of this magnitude or to state categorically which method is "correct." Within the boundary layer, the region of principal interest, the methods agree remarkably well.

Finally, a major effect of the strong nonlinearity is a mean (0, 0) component that distorts the base flow. Figure 17 shows that the PSE and DNS calculations both predict large (5%) distortions of the

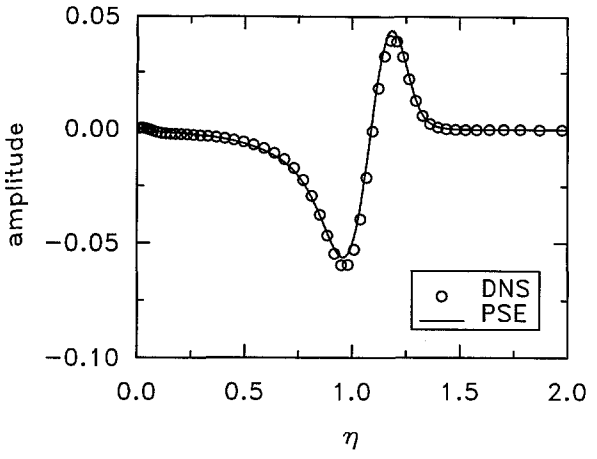

Figure 17. Case 3: Nonlinearly generated mean temperature distortion versus η at $Re_L = 1050$.

base temperature distribution near the critical layer. Disagreement between the methods is roughly 6% at the points of maximum distortion. The reason for the disparity is presently unknown.

Case 4: Sharp Cone, Mach 6.8 Nonparallel Flow, Three-Dimensional Linear Disturbance. In this final validation case we consider the high-speed boundary-layer flow along an axisymmetric sharp cone, which is forced to excite two symmetric oblique (helical) second-mode disturbances. The geometry and the flow parameters given below are chosen to correspond approximately to the stability experiment of Stetson *et al.* (1983) in a hypersonic wind tunnel with a free-stream Mach number of 8:

$$\varphi = 7^\circ \quad \text{(constant)}, \qquad M_e = 6.8, \qquad T_e^* = 71 \text{ K}. \tag{36}$$

We assume that the boundary-layer edge conditions remain constant, a reasonable approximation except near the tip of the cone, a region excluded in the present simulations. The PSE calculation spans from $700 \leq Re_L \leq 1800$. To limit the size of the DNS computation, we consider only the region corresponding to $1013 \leq Re_L \leq 1536$. At the DNS inflow boundary, the disturbance parameters are

$$\begin{gathered} F = 2.094 \times 10^{-4}, \\ n = 13 \qquad (\beta_0 = 1.1736,\ R_0 = 11.077), \\ \varepsilon = 0.001, \end{gathered} \tag{37}$$

and $\delta_{\text{in}}^*/L^* = 11.17$. Whereas the geometry and flow parameters correspond to the experiment of Stetson *et al.* (1983), the disturbance parameters were selected somewhat arbitrarily. The dimensionless frequency given in (37) corresponds to a physical frequency of 180 kHz, considerably higher than the dominant 102 kHz frequency observed in the experiment. The higher frequency was selected for this validation case because its entire instability region, including the lower and upper branch neutral points, is contained within a fairly short streamwise region, one of (almost) reasonable size for a DNS calculation of modest computational effort. There is nothing sacred about the particular choice of $n = 13$, except that it yields an unstable mode of a sizeable obliqueness angle (24.66° at the DNS inflow boundary) for the given frequency.

Figure 18 presents the evolution of the amplitudes of each of the five components of the fundamental (1, 1) mode for $700 \leq Re_L \leq 1500$. In this case the buffer region for the DNS calculation is not shown. As in Case 2, the PSE calculation is performed in the linear mode, in which case amplitude is arbitrary. For the comparisons below, the maximum densities of the PSE and DNS calculations are equated at the DNS inflow plane, and all other quantities are scaled accordingly. The agreement between the DNS and PSE results is, in general, quite good. The kinks in the u' maxima curve at $Re_L = 1120$ and the w' maxima curve at $Re_L = 1280$ are due to the double-humped structure of the disturbance shown in Figure 19. Remarkably, the DNS and PSE results predict the shift of the global maximum from one hump to the other at precisely the same values of Re_L. There is some discrepancy

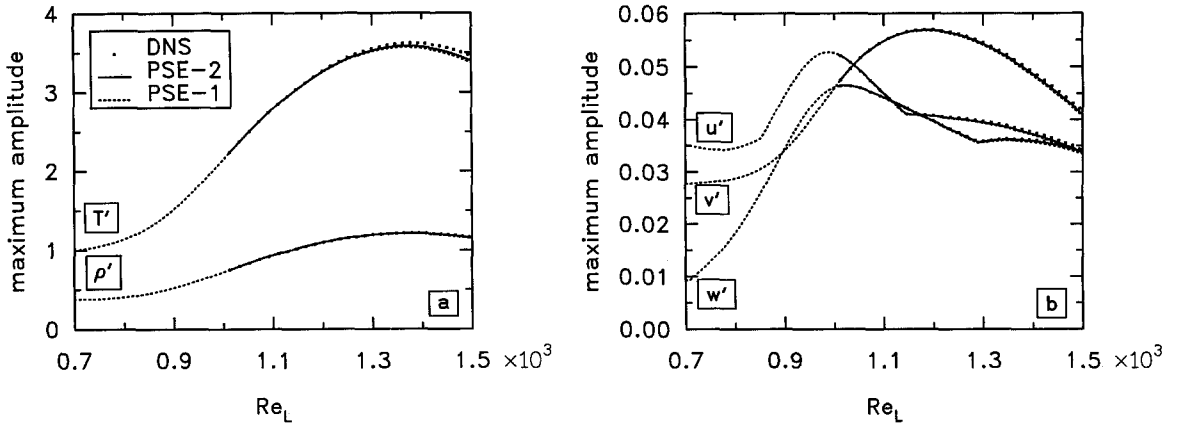

Figure 18. Case 4: PSE and DNS disturbance amplitude maxima versus Re_L for cone case: (a) T' and ρ' and (b) u', v', and w'. Two distinct PSE results differ only in the method by which wall-normal derivatives of the base flow are computed.

in the DNS and PSE maxima, which is most significant in the temperature, and which increases with streamwise distance. To eliminate one potential source of disagreement for this comparison, the laminar base flow $\mathbf{Q}^0$ along the cone was obtained for both the PSE and DNS calculations from the spectrally accurate BL code of Pruett and Streett (1991) and Pruett (1993). The remaining sources of disagreement may be either physical or numerical or a combination. We remind the reader that the governing equations, the far-field boundary conditions, and the discretions of the two methods differ, to mention but a few of many subtle differences whose effects may be cumulative. Because the flow is sensitive to seemingly imperceptible changes, it is somewhat pointless to try to isolate the sources of disagreement. Perhaps it is more instructive to demonstrate this flow-field sensitivity. In Figure 18 two sets of PSE results are shown. The two sets differ only in the method by which derivatives of the base state were obtained. In the first set all derivatives were computed internally in the PSE code to fourth-order accuracy. In the second set the derivatives u_z, u_{zz}, T_z, and T_{zz} were computed to spectral accuracy in the BL code and were subsequently passed to the PSE code. Figure 20 compares the first and second derivatives of the temperature as computed by the BL and PSE codes. At worst, the temperature derivatives computed by the two methods differ by less than 0.001, and, in the graphical format, they are indistinguishable. Moreover, velocity derivatives obtained by the two methods agree everywhere to more than four significant digits. Nevertheless, the cumulative effect of these seemingly insignificant differences between derivative profiles is discernible in Figure 18. This inconsistency did not arise for the flat-plate test cases studied previously, for which the base flow is

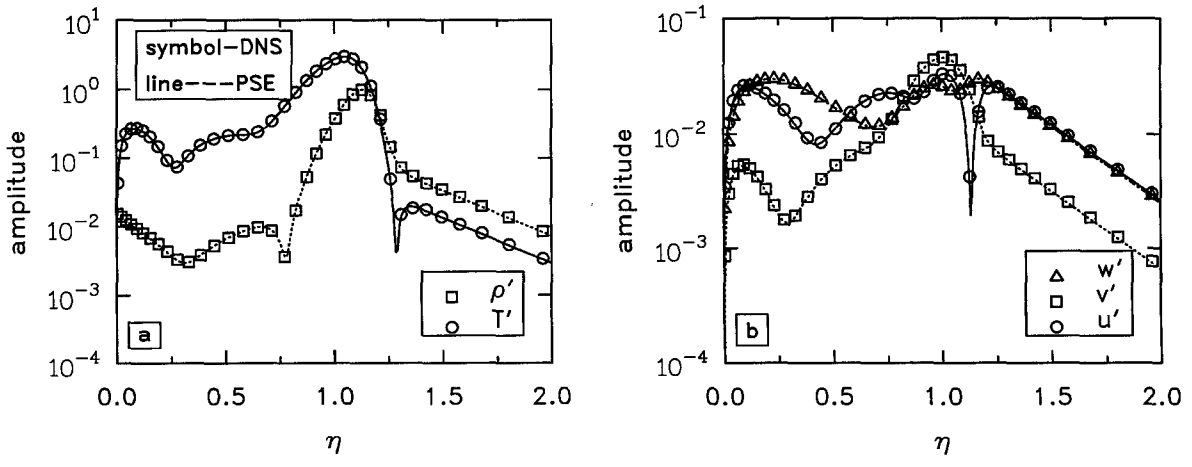

Figure 19. Case 4: Structure at $Re_L = 1291$ of (a) T' and ρ' and (b) u', v', and w'.

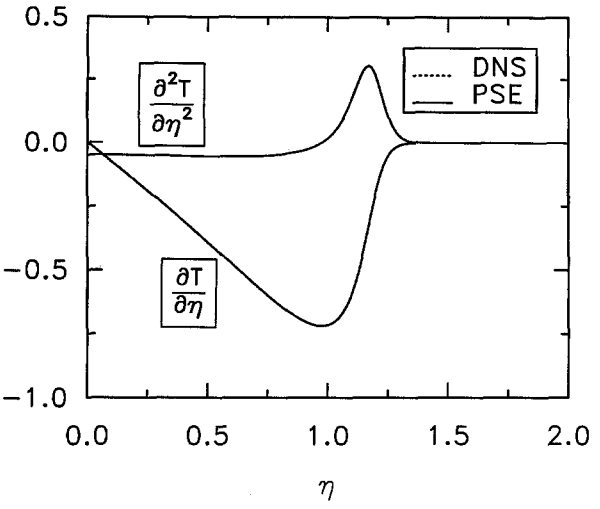

Figure 20. Case 4: Wall-normal derivatives of base temperature.

obtained from a similarity solution whose derivatives can be obtained semianalytically. These results reveal the extreme sensitivity of the stability of high-speed wall-bounded flows to changes in the base state and underscore the necessity of numerical methods of the highest accuracy for such problems.

Before concluding, we offer a few comments on the computational resources required by the present algorithm. DNS is, in general, an expensive research tool. Cases 3 and 4 of this section consumed approximately 40 and 150 hours, respectively, on a single processor of a Cay Y-MP. It is estimated that spatial DNS of the complete laminar-breakdown process for a high-speed boundary-layer flow will require at least 2000 Cray-2 hours and at least 256 megawords of memory. Needless to say, such a tool is not for routine use at the present time. Nevertheless, spatial DNS is invaluable as a means of validating less-expensive approximate methods (e.g., PSE and LES) and for building high-fidelity data bases of transitioning flows, from which transition modelers can construct simplified models. With continued algorithm refinements, supercomputer advancements, and massively parallel impelementations, we believe spatial DNS of transition to turbulence will be practical and routine well within a decade.

6. Conclusions

A highly accurate algorithm has been developed for the direct numerical simulation (DNS) of forced, spatially evolving instability waves in high-speed wall-bounded flows. To minimize dissipation and dispersion errors, the fully explicit algorithm exploits both spectral collocation and high-order central compact-difference techniques. In its present form the algorithm allows for three-dimensional flow along two-dimensional or axisymmetric bodies. Of particular interest in this work are the flat-plate and the sharp-cone geometries.

Part 1 of this paper deals primarily with thorough validation of the DNS scheme by comparisons with results obtained from classical linear stability theory (LST) and from the parabolized stability equation (PSE) method. Test cases examine forced two-dimensional second-mode instability waves in Mach 4.5 flat-plate boundary-layer flows and three-dimensional second-mode waves in a Mach 6.8 flow along a sharp cone. From these validation studies, several insights emerge that pertain both to the numerical methods and to the physical problems addressed. First, for the Mach numbers of the test cases, the streamwise resolution needed to obtain good agreement with theoretical results was higher than anticipated. With sixth-order streamwise accuracy, approximately 12 and 16 grid points per wavelength were required in order to extract the growth rate of a monochromatic disturbance to three and four place accuracy, respectively. Second, for nonparallel flows, consistent inflow conditions for the DNS can be obtained from the PSE method, whereas inflow conditions derived from LST are fundamentally inconsistent due to the parallel-flow approximation of LST. Third, at these high Mach numbers, the stability of the boundary layers was found to be sensitive to

the slightest (almost imperceptible) change in the base state. Fourth, for low-amplitude (linear) disturbances the agreement between the PSE method and the DNS results was near perfect in terms of both the amplitude and the structure of the disturbances. Fifth, for large-amplitude (nonlinear) disturbances, agreement between the two methods was near-perfect for the fundamental and good for engineering purposes for the higher harmonics, with the tendency towards greater disagreement the higher the harmonic. Finally, the generally close agreement between DNS and PSE results convincingly demonstrates the potential of the PSE method as a reliable new tool for analysis of hydrodynamic stability in high-speed wall-bounded flows.

At present there is a great need for experimental studies of stability and transition in high-speed boundary-layer flows. Until such experiments are accomplished, the only available source of detailed flow-field information for high-speed transitional flows is DNS. The development and validation of the present DNS algorithm thus fills a void in the national capability in the area of transition research. Using this new tool, Part 2 of this work will examine in detail the laminar breakdown of a perturbed high-speed boundary-layer flow along a cone.

Acknowledgments

The authors wish to acknowledge the many colleagues whose insights, suggestions, or comments contributed to this work. Among these are Dr. Craig Streett, Dr. Shlomo Ta'asan, Dr. Saad Ragab, Dr. Harold Atkins, and Chris Kennedy. The authors are also grateful to Dr. Leslie Mack for his pioneering work in the stability of high-speed flows and for permission to use Figure 10.

References

N.A. Adams and L. Kleiser. Numerical simulation of transition in a compressible flat-plate boundary layer. In *Transitional and Turbulent Compressible Flows—1993* (L.D. Kral and T.A. Zang, eds.). FED, Vol. 151. ASME, New York, 1993, pp. 101–110 (presented at the Fluids Engineering Conference, Washington, DC, June 20–24, 1993).

A. Bayliss, L. Maestrello, P. Parikh, and E. Turkel. Wave phenomena in a high Reynolds number compressible boundary layer. In *Stability for Time Dependent and Spatially Varying Flows* (D.L. Dwoyer and M.Y. Hussaini, eds.). Springer-Verlag, New York, 1985, pp. 188–205.

C. Canuto, A. Quateroni, M.Y. Hussaini, and T.A. Zang. *Spectral Methods in Fluid Dynamics*. Springer-Verlag, Berlin, 1988.

M.H. Carpenter, D. Gottlieb, and S. Abarbanel. The stability of numerical boundary treatments for compact high-order finite-difference schemes. ICASE Report No. 91-71, 1991.

C.-L. Chang. Unpublished personal communication, 1993.

C.-L. Chang, M.R. Malik, G. Erlebacher, and M.Y. Hussaini. Compressible stability of growing boundary layers using parabolized stability equations. AIAA Paper 91-1636, 1991.

D.F. DeSanto and H.B. Keller. Numerical studies of transition from laminar to turbulent flow over a flat plate. *J. Soc. Indust. Appl. Math.*, Vol. 10, No. 4, 1962, pp. 569–595.

S.P.G. Dinavahi and C.D. Pruett. Analysis of direct numerical simulation data of a Mach 4.5 transitional boundary-layer flow. In *Transitional and Turbulent Compressible Flows—1993* (L.D. Kral and T.A. Zang, eds.). FED, Vol. 151. ASME, New York, 1993, pp. 147–153 (presented at the Fluids Engineering Conference, Washington, DC, June 20–24, 1993).

W. Eissler and H. Bestek. Spatial numerical simulations of nonlinear transition phenomena in supersonic boundary layers. In *Transitional and Turbulent Compressible Flows—1993* (L.D. Kral and T.A. Zang, eds.). FED, Vol. 151. ASME, New York, 1993, pp. 69–76 (presented at the Fluids Engineering Conference, Washington, DC, June 20–24, 1993).

N.M. El-Hady, T.A. Zang, and U. Piomelli. Dynamic subgrid-scale modeling for high-speed transitional boundary layers. In *Engineering Applications of Large Eddy Simulations—1993* (S.A. Ragab and U. Piomelli, eds.). FED, Vol. 162. ASME, New York, 1993 (presented at the Fluids Engineering Conference, Washington, DC, June 20–24, 1993).

G. Erlebacher and M.Y. Hussaini. Numerical experiments in supersonic boundary-layer stability. *Phys. Fluids A*, Vol. 2, No. 1, 1990, pp. 94–104.

H. Fasel, A. Thumm, and H. Bestek. Direct numerical simulation of transition in supersonic boundary layers: oblique breakdown. In *Transitional and Turbulent Compressible Flows—1993* (L.D. Kral and T.A. Zang, eds.). FED, Vol. 151. ASME, New York, 1993, pp. 77–92 (presented at the Fluids Engineering Conference, Washington, DC, June 20–24, 1993).

N. Gilbert and L. Kleiser. Near-wall phenomena in transition to turbulence. In *Near-Wall Turbulence: 1988 Zoran Zaric Memorial Conference* (S.J. Kline and N.H. Afgan, eds.). Hemisphere, Washington, DC, 1990, pp. 17–27.

B. Gustafsson. The convergence rate for difference approximations to mixed initial boundary-value problems. *Math. Comp.*, Vol. 29, No. 130, 1975, pp. 396–406.

L. Kleiser and T.A. Zang. Numerical simulation of transition in wall-bounded shear flows. *Annu. Rev. Fluid Mech.*, Vol. 23, 1991, pp. 495–537.

L.D. Kral. Numerical Investigation of Transition Control of a Flat Plate Boundary Layer. Ph.D. thesis, University of Arizona, 1988.

S.K. Lele. Compact finite difference schemes with spectral-like resolution. Center for Turbulence Research Manuscript 107, Stanford University, April 1990.

L.M. Mack. Boundary-layer linear stability theory. In *Special Course on Stability and Transition of Laminar Flow* (R. Michel, ed.). AGARD Report No. 709, 1984, pp. 3.1–3.81.

L. Maestrello, A. Bayliss, and R. Krishnan. On the interaction between first and second-mode waves in a supersonic boundary layer. *Phys. Fluids A*, Vol. 3, No. 12, 1991, pp. 3014–3020.

L.L. Ng and G. Erlebacher. Secondary instabilities in compressible boundary layels. *Phys. Fluids A*, Vol. 4, No. 4, 1992, pp. 710–726.

L.L. Ng and T.A. Zang. Secondary instability mechanisms in compressible, axisymmetric boundary layers. *AIAA J.*, Vol. 31, No. 9, Sept. 1993, pp. 1605–1610.

J. Nordstrom. The influence of open boundary conditions on the convergence to steady state for the Navier–Stokes equations. *J. Comput. Phys.*, Vol. 85, 1989, pp. 210–244.

X. Normand and M. Lesieur. Direct and large-eddy simulations of transition in the compressible boundary layer. *Theoret. Comput. Fluid Dynamics*, Vol. 3, 1992, pp. 231–252.

T.J. Poinsot and S.K. Lele. Boundary conditions for direct simulations of compressible viscous flows. *J. Comput. Phys.*, Vol. 101, 1992, pp. 104–129.

C.D. Pruett. On the accurate prediction of the wall-normal velocity in compressible boundary-layer flow. *Internat. J. Numer. Methods Fluids*, Vol. 16, 1993, pp. 133–152.

C.D. Pruett and C.-L. Chang. A comparison of PSE and DNS for high-speed boundary-layer flows. In *Transitional and Turbulent Compressible Flows—1993* (L.D. Kral and T.A. Zang, eds.). FED, Vol. 151. ASME, New York, 1993, pp. 57–67 (presented at the Fluids Engineering Conference, Washington, DC, June 20–24, 1993).

C.D. Pruett and C.L. Streett. A spectral collocation method for compressible, non-similar boundary layers. *Internat. J. Numer. Methods Fluids*, Vol. 13, No. 6, 1991, pp. 713–737.

C.D. Pruett and T.A. Zang. Direct numerical simulation of laminar breakdown in high-speed, axisymmetric boundary layers. *Theoret. Comput. Fluid Dynamics*, Vol. 3, No. 6, 1992, pp. 345–367.

M. Rai and P. Moin. Direct numerical simulation of transition and turbulence in a spatially evolving boundary layer. AlAA Paper No. 91-1607, 1991.

K.F. Stetson and R.L. Kimmel. On the breakdown of a hypersonic laminar boundary layer. AIAA Paper 93-0896, 1993.

K.F. Stetson, E.R. Thompson, J.C. Donaldson, and L.G. Siler. Laminar boundary-layer stability experiments on a cone at Mach 8. Part 1: Sharp cone. AIAA Paper 83-1761, 1983.

C.L. Streett and M.G. Macaraeg. Spectral multi-domain for large-scale fluid dynamic simulations. *Appl. Numer. Math.*, Vol. 6, 1989/90, pp. 123–139.

K.W. Thompson. Time dependent boundary conditions for hyperholic systems. *J. Comput. Phys.*, Vol. 68, 1987, pp. 1–24.

A. Thumm. Numerische Untersuchungen zum laminar-turbulenten Stroemungsumschlag in transsonischen Grenzschictstroemunge. Ph.D. thesis, Universitaet Stuttgart, 1991.

A. Thumm, W. Wolz, and H. Fasel. Numerical simulation of spatially growing three-dimensional disturbance waves in compressible boundary layers. In *Laminar-Turbulent Transition. IUTAM Symposium, Toulouse, France, 1989* (D. Arnal and R. Michel, eds.). Springer-Verlag, Berlin, 1990, pp. 303–308.

L.N. Trefethen. Group velocity in finite difference schemes. *SIAM Rev.*, Vol. 24, No. 2, 1982, pp. 113–136.

R. Vichnevetsky. Invariance theorems concerning reflection at numerical boundaries. *J. Comput. Phys.*, Vol. 63, 1986, pp. 268–282.

F.M. White. *Viscous Fluid Flow*. McGraw-Hill, New York, 1974, pp. 347–350.

J.H. Williamson. Low-storage Runge–Kutta schemes. *J. Comput. Phys.*, Vol. 35, 1980, pp. 48–56.

T.A. Zang, C.-L. Chang, and L.L. Ng. The transition prediction toolkit: LST, SIT, PSE, DNS, and LES. Fifth Symposium on Numerical and Physical Aspects of Aerodynamic Flows, January 1992.